Structural Basis of PML-RARA Oncoprotein Targeting by Arsenic Unravels a Cysteine Rheostat Controlling PML Body Assembly and Function

Pierre Bercier, Qian Qian Wang, Ning Zang, Jie Zhang, Chang Yang, Yasen Maimaitiyiming, Majdouline Abou-Ghali, Caroline Berthier, Chengchen Wu, Michiko Niwa-Kawakita, et al.

RESEARCH ARTICLE

Structural Basis of PML-RARA Oncoprotein Targeting by Arsenic Unravels a Cysteine Rheostat Controlling PML Body Assembly and Function

Pierre Bercier[1,2], Qian Qian Wang[3,4,5], Ning Zang[4,6], Jie Zhang[4,6], Chang Yang[3,4,5], Yasen Maimaitiyiming[3,4,5], Majdouline Abou-Ghali[1,2], Caroline Berthier[1], Chengchen Wu[1,2], Michiko Niwa-Kawakita[1,2], Thassadite Dirami[1,2], Marie-Claude Geoffroy[1,2], Omar Ferhi[1,2], Samuel Quentin[2], Shirine Benhenda[2], Yasumitsu Ogra[7], Zoher Gueroui[8], Chun Zhou[4,6], Hua Naranmandura[3,4], Hugues de Thé[1,2,9], and Valérie Lallemand-Breitenbach[1,2]

ABSTRACT PML nuclear bodies (NB) are disrupted in PML-RARA–driven acute promyelocytic leukemia (APL). Arsenic trioxide (ATO) cures 70% of patients with APL, driving PML-RARA degradation and NB reformation. In non-APL cells, arsenic binding onto PML also amplifies NB formation. Yet, the actual molecular mechanism(s) involved remain(s) elusive. Here, we establish that PML NBs display some features of liquid–liquid phase separation and that ATO induces a gel-like transition. PML B-box-2 structure reveals an alpha helix driving B2 trimerization and positioning a cysteine trio to form an ideal arsenic-binding pocket. Altering either of the latter impedes ATO-driven NB assembly, PML sumoylation, and PML-RARA degradation, mechanistically explaining clinical ATO resistance. This B2 trimer and the C213 trio create an oxidation-sensitive rheostat that controls PML NB assembly dynamics and downstream signaling in both basal state and during stress response. These findings identify the structural basis for arsenic targeting of PML that could pave the way to novel cancer drugs.

SIGNIFICANCE: Arsenic curative effects in APL rely on PML targeting. We report a PML B-box-2 structure that drives trimer assembly, positioning a cysteine trio to form an arsenic-binding pocket, which is disrupted in resistant patients. Identification of this ROS-sensitive triad controlling PML dynamics and functions could yield novel drugs.

INTRODUCTION

Promyelocytic leukemia (PML) protein organizes the formation of stress-sensitive membrane-less organelles (MLO): PML nuclear bodies (NB). PML controls various biological functions, such as apoptosis, senescence, or stem cell self-renewal (1, 2). PML may elicit these functions by scaffolding the spherical shells of NBs, which subsequently act as hubs of posttranslational modifications, in particular sumoylation, for the broad range of proteins trafficking through NB inner cores. PML NBs are disrupted in acute promyelocytic leukemia (APL) driven by the PML-RARA oncogenic fusion protein. PML protein expression and NB formation are also downregulated in many other cancers (3–5). The combination of arsenic trioxide (ATO) and retinoic acid treatments drives APL cure by enforcing PML-RARA degradation and PML NB reassembly, subsequently leading to the activation of a senescence-like program in APL cells (3). ATO, which as single therapy cures 70% of patients with APL (6, 7), directly binds PML-RARA and PML proteins (8, 9). While ATO-driven PML-RARA degradation is biochemically well understood (10), ATO-enforced NB assembly remains understudied. Formation of PML intermolecular disulfide bonds was reported in response to ATO (8) and arsenic was proposed to replace a Zn^{2+} ion in the RING finger (9). However, ATO effects on NB assembly remain imperfectly understood.

Biogenesis of MLO has been revisited through the prism of liquid–liquid phase separation (LLPS). Biomolecular condensates may arise by multivalent weak interactions between proteins, or proteins and RNAs, which demix from the surrounding media to form spherical structures, maintained as an equilibrium despite dynamic exchange of their components (11, 12). LLPS has been proposed to increase kinetics of biochemical reactions among its constituents and could contribute to disease initiation (13, 14). In leukemia, chimeric transcription factors may condensate through LLPS, resulting in aberrant 3D chromatin structures and contributing to their aberrant transcriptional activity (15, 16). *In vitro*, chimeric GFP-polySUMO proteins condense in droplets through LLPS when combined with chimeric proteins containing repetitions of SUMO-interacting motif (SIM; ref. 17). Yet, PML sumoylation is dispensable for PML NB assembly (18, 19) and the contribution of LLPS in PML NB assembly still remains elusive.

[1]Center for Interdisciplinary Research in Biology (CIRB), Collège de France, CNRS, INSERM, Université PSL, Paris, France. [2]GenCellDis, Inserm U944, CNRS UMR7212, Université Paris Cité, Paris, France. [3]Department of Hematology of First Affiliated Hospital, School of Medicine, Zhejiang University, Hangzhou, China. [4]Public Health, School of Medicine and Department of Toxicology, Zhejiang University, Hangzhou, China. [5]College of Pharmaceutical Sciences, Zhejiang University, Hangzhou, China. [6]Department of Pathology, Sir Run Run Shaw Hospital, Zhejiang University School of Medicine, Hangzhou, China. [7]Graduate School of Pharmaceutical Sciences, Chiba University, Chiba, Japan. [8]Department of Chemistry, École Normale Supérieure, PSL University, Sorbonne Université, CNRS, Paris, France. [9]Hematology Laboratory, Hôpital St Louis, AP/HP, Paris, France.

Note: P. Bercier, Q.Q. Wang, and N. Zang are the co–first authors of this article.

C. Zhou, H. Naranmandura, H. de Thé, and V. Lallemand-Breitenbach are the co–senior authors of this article.

Corresponding Authors: Valérie Lallemand-Breitenbach, Center for Interdisciplinary Research in Biology, U1050, Collège de France, 11 Place Marcelin Berthelot, Paris 75231 Cedex 05, France. E-mail: valerie.lallemand@inserm.fr; Hugues de Thé, hugues.dethe@inserm.fr; Chun Zhou, Department of Public Health, Zhejiang University School of Medicine, Hangzhou, Zhejiang 310058, China. E-mail: chunzhou@zju.edu.cn; and Hua Naranmandura, narenman@zju.edu.cn

Cancer Discov 2023;13:1–18

doi: 10.1158/2159-8290.CD-23-0453

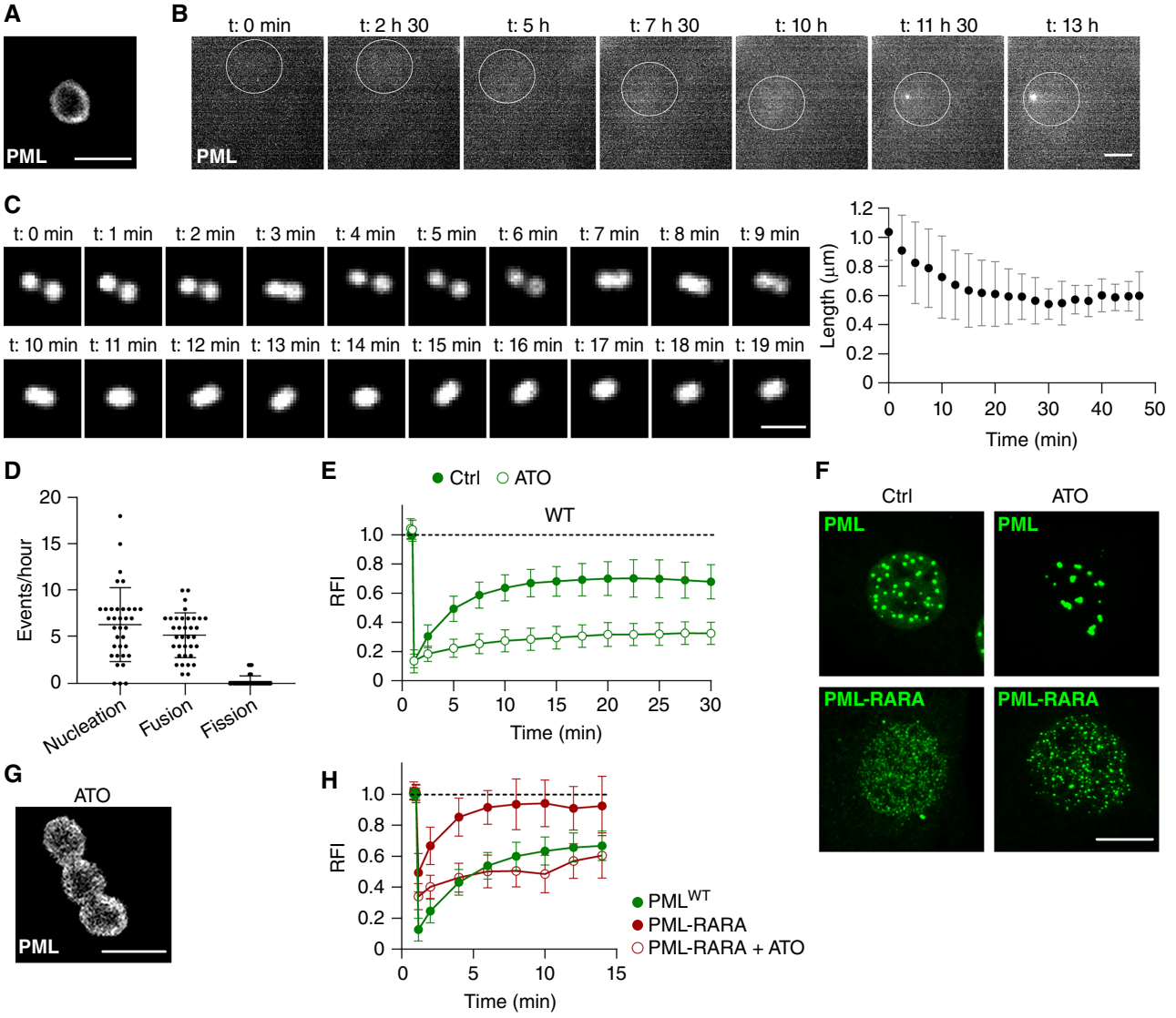

Figure 1. PML NBs display hallmarks of LLPS and switch to gel-like features upon ATO exposure. **A,** STED analysis uncovers the typical spherical core-shell PML NB. Scale bar, 1 µm. **B,** Time-lapse analysis of PML NB apparition upon GFP-PML^{WT} expression in *Pml*^{KO} MEFs. The white circle indicates the nucleus. Representative data from three independent experiments. Scale bar, 5 µm. **C,** PML NBs undergo fusion with spherical relaxation, similar to liquid-like droplets. Representative time-lapse of PML NB fusion (left) and quantification of effective viscosity (right). Mean values ± SD of $n = 21$ fusion events in independent cells from three independent experiments. Scale bar, 1 µm. **D,** Quantification of PML NB nucleation, fusion, and fission events over 1 hour. Mean value ± SD of $n = 37$ cells from five independent experiments. **E,** FRAP analyses of GFP-PML^{WT} dynamics at NBs in control (Ctrl) or ATO-treated MEFs (1 µmol/L, 30 minutes). Mean value ± SD. Number of NBs assessed Ctrl ($n = 36$), ATO ($n = 28$), from at least five independent experiments. WT, wild-type. **F,** Confocal analysis of PML NBs in GFP-PML^{WT} or GFP-PML-RARA MEFs treated with 1 µmol/L of ATO for 1 hour. Scale bar, 5 µm. **G,** STED analysis demonstrating incomplete PML NB fusion upon ATO in PML^{KO} MEFs s. Scale bar, 1 µm. **H,** Comparison between GFP-PML^{WT} and GFP-PML-RARA dynamics at NBs by FRAP. ATO treatment (1 µmol/L, 30 minutes) induces a liquid- to gel-like transition of GFP-PML-RARA. Mean value ± SD. Number of dots assessed PML ($n = 36$), PML-RARA ($n = 20$), PML-RARA+ATO ($n = 37$), from at least five independent experiments. RFI, Relative fluorescence intensity.

In this study, we elucidate the crystal structure of PML B-box 2 (B2) and identify an α-helix that mediates B2 trimerization through hydrophobic interactions, controlling PML NB assembly and PML dynamics. This α-helix–mediated trimer organizes a triad of free C213 cysteines to which trivalent arsenic covalently docks, switching PML NBs from liquid-like to gel-like bodies. B2 trimerization and C213 are mandatory for PML-mediated function, such as oxidative stress response *in vivo*, as well as ATO-triggered PML-RARA degradation, uncovering the very first step by which ATO achieves antileukemia cure.

RESULTS

PML NBs Switch from Liquid-Like to Gel-Like Structures upon ATO

PML NBs are spherical membrane-less organelles forming core-shell structures (Fig. 1A). To determine whether PML assembly in NBs reflects LLPS, we stably expressed GFP-PML-III (here after named GFP-PML) in *Pml*^{KO} mouse embryonic fibroblasts (MEF) and assessed hallmarks of liquid-like MLO: solubility limit, fusion/relaxation, and dynamic exchange.

First, we examined whether PML could demix from the nucleoplasm above a concentration threshold by live-cell imaging following retroviral cell transduction. PML was initially homogeneously distributed in the nucleoplasm, but as GFP-PML expression increased, the first PML NB appeared (Fig. 1B). NBs then became more numerous, while the diffuse fraction remained constant (Supplementary Fig. S1A). Similarly, the number of PML NBs increases with PML transcriptional activation upon IFNα treatment (20, 21). Thus, PML demixes from a diffuse nucleoplasmic fraction into NBs above a concentration threshold. Live-cell imaging revealed that two PML NBs can fuse and relax in a novel single spherical body, supporting liquid-like behavior of PML NBs (Fig. 1C; Supplementary Movie S1). In these experiments, analysis of the relaxation curves and plotting the size of fusing PML NBs as a function of time, allowed extraction of the diffusion coefficient of PML proteins and a NB capillary viscosity in the 10^3 Pa·s range (Supplementary Fig. S1B; ref. 22), comparable to that of nucleoli or nuclear speckles (23, 24). We then quantified the number of events of GFP-PML nucleation from the diffuse nucleoplasmic fraction, of PML NB fusions or fissions (Fig. 1D). Fusion events occurrence were similar to nucleation ones, maintaining a mean number of 40 PML NBs per nucleus, while fission events were rare. We then assessed the dynamics of PML NB assembly by fluorescence recovery after photobleaching (FRAP). As reported, PML protein dynamically exchanges between the nucleoplasm and NBs, with a half recovery time ($t_{1/2}$) of 3.2 minutes (Fig. 1E; refs. 8, 25, 26). Taken together, these results establish that PML NBs exhibit some hallmarks of LLP-separated condensates. However, the residence time of PML at NBs is much longer than other MLO nucleators, such as those driving Cajal bodies, speckles, or nucleoli (minutes vs. seconds), indicating higher interaction affinity between PML proteins at NBs. Moreover, 30% of the GFP-PML fluorescence bleached at NBs never recovers (Fig. 1E), implying that two PML fractions coexist at NBs, one exchanging with the surrounding nucleoplasm, the other remaining immobile. Together with the existence of the core-shell structure, this challenges a pure LLPS of PML proteins as a simple model of NB assembly.

ATO exposure rapidly increased PML NB–associated fraction at the expense of the diffuse one and PML NB assembly dynamics dramatically dropped, so that almost all PMLs became immobilized (Fig. 1E). Live-cell imaging and super-resolution microscopy showed that PML NBs tend to aggregate without achieving complete fusion, forming PML NB strings, consistent with an increase in their viscoelasticity (Fig. 1F and G; Supplementary Movie S2). Thus, ATO triggers the transition from liquid-like to gel-like PML NBs.

PML fusion to RARA altered its distribution in the nucleus, as GFP-PML-RARA localized into many tiny dots with diameter below 100 nm in Pml^{KO} MEFs (refs. 8, 27; Fig. 1F). The basal dynamics of GFP-PML-RARA at these microdots was increased compared with PML at NBs, with a $t_{1/2}$ of 1.37 minutes and, importantly, no immobile fraction (Fig. 1H). Yet, here again, ATO treatment drastically decreased PML-RARA exchange rates, closer to the dynamics of PML. Thus, ATO therapy drives the gel-like transition of both PML- or PML-RARA–driven condensates.

PML NB Assembly Requires the B2 Box Domain Rather than Disulfide Bridges

Arsenic atoms may bind sulfhydryl groups, primarily targeting cysteine residues in cells. Within PML, arsenic was proposed either to directly target cysteines of the RING finger, in which arsenic would replace the structuring zinc atom, or B2, another zinc finger domain that contains adjacent cysteines: C212 and C213 (8, 9). We first assessed the role of free cysteines in NB formation by using N-ethyl-maleimide (NEM), which alkylates cysteine residues with a freely accessible -SH group. Pretreatment with NEM blocked both basal PML NB assembly and ATO-enforced PML NB formation (Fig. 2A). Conversely, treatment with ATO precluded subsequent NEM-induced disorganization of PML NBs. Thus, the cysteine(s) required for baseline NB assembly are accessible, not involved in zinc coordination, and likely the same as those targeted by ATO. This does not support the RING finger as being the primary ATO target site.

ATO exposure induces ROS production due to glutathione scavenging and mitochondrial poisoning (28–30). We previously showed that disulfide bonds may link PML monomers, driving their covalent multimerization upon oxidative stress (8). We sought to disentangle the respective contribution of direct arsenic binding or ATO-enhanced disulfide bonds in PML NB assembly. By homology with other TRIpartite Motif (TRIM) proteins, the C213 residue is likely not involved in zinc coordination (31). We thus focused on both C213 and C389, the latter being an oxidation-sensitive residue implicated in oncoprotein targeting (32, 33). PML intermolecular disulfide bonds can be assessed by Western blot analysis in nonreducing conditions, which revealed high molecular weight PML multimers, whose abundance sharply increased upon ATO or H_2O_2 (Fig. 2B; Supplementary Fig. S1C; ref. 8), but were lost under reducing conditions (Supplementary Fig. S1C and S1D). C389S mutation impaired ATO-induced disulfides, but only modestly affected those induced by H_2O_2, while C213A decreased PML intermolecular-bound species induced by both ATO and H_2O_2. The double C213A/C389S mutation completely abrogated the formation of these PML multimers (Fig. 2B).

Following PML NB assembly, PML becomes sumoylated (18, 21, 34). ATO-induced gel-like NBs are associated with a massive increase in PML sumoylation (Fig. 2B). Interestingly, PML^{C213A} mutants were defective for sumoylation, while PML^{C389S} did not affect basal or ATO-induced SUMO conjugation of PML. We then assessed the localization patterns of wild-type or mutant PML upon those stresses. Surprisingly, in contrast to ATO, H_2O_2 did not significantly alter the diffuse nuclear fraction of wild-type (WT) PML, nor increase the NB-associated fraction, suggesting that intermolecular disulfides are not responsible for the gel-like transition (Fig. 2C). Critically, C213A or C389S mutations had very different effects on NB formation (Fig. 2C). While defective for ATO-induced disulfide, PML^{C389S} NBs and diffuse fraction were identical to those of WT PML, including full ATO sensitivity. In contrast, PML^{C213A} remained mainly diffuse, with a single enlarged body, unaffected by ATO. Taken together, these results indicate that C213 is essential for PML NB assembly, but intermolecular disulfide bonds mediated by C213 or C389 are not, and suggest that C213 may directly contribute to arsenic binding.

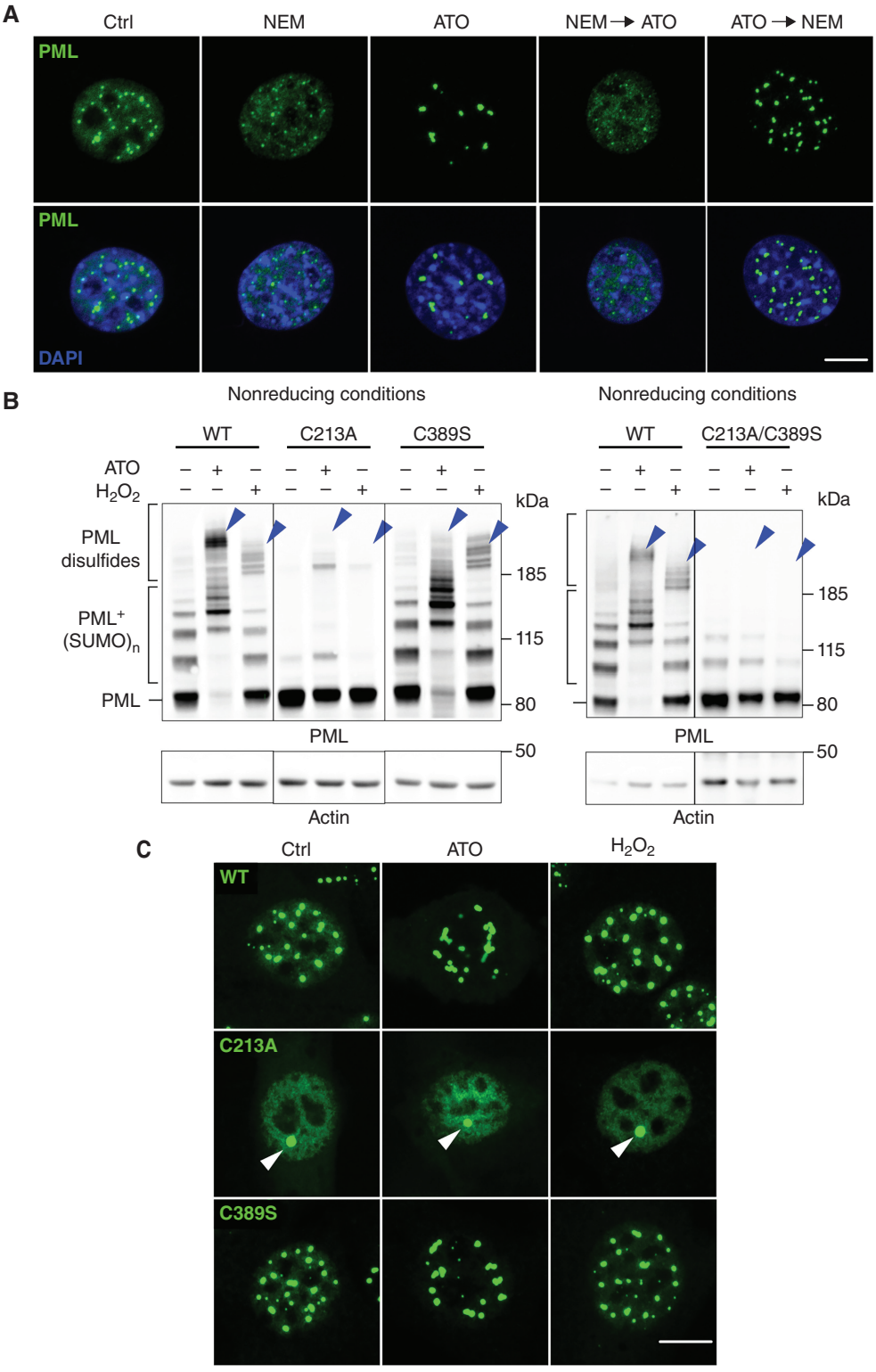

Figure 2. PML NB assembly depends on C213 in B2 domain, but not on C389-mediated intermolecular disulfide bonds. **A,** Confocal analysis of PML NB formation following cysteine alkylation with NEM (10 μmol/L, 1 hour) or ATO (1 μmol/L, 1 hour) used alone or sequentially in GFP-PML^{WT} MEFs. Scale bar, 5 μm. Ctrl, control. **B,** Western blot analysis (nonreducing conditions) of PML disulfide bond formation in MEFs expressing HA-PML^{WT} or PML cysteine mutants, treated or not with ATO (10 μmol/L, 1 hour) or H_2O_2 (500 μmol/L, 1 hour). Brackets: SUMO-conjugated or intermolecular disulfide-bound PML. Blue arrowheads, intermolecular disulfide-bound PML. Molecular weight (kDa). **C,** Confocal analysis of PML NBs upon ATO (1 μmol/L, 1 hour) or H_2O_2 (500 μmol/L, 1 hour) exposure in HA-PML^{WT}- or cysteine mutant–expressing MEFs. Arrowheads, single NB in HA-PML^{C213A}-expressing MEFs. Scale bar, 5 μm.

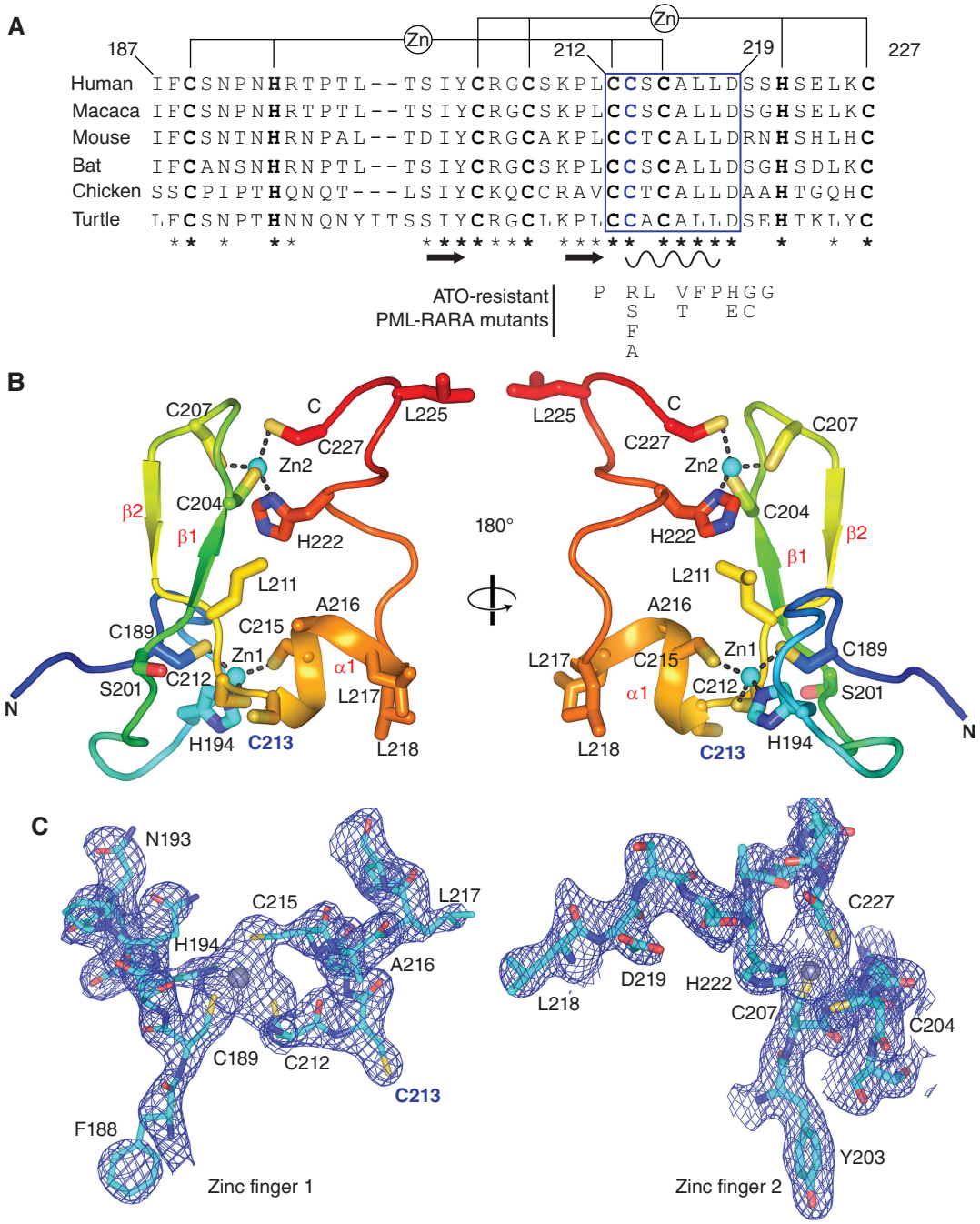

Figure 3. Uncovering PML B2 structure. **A,** Conservation of PML B2 box through evolution. Top, putative position of the two zinc fingers intertwined in a cross-brace. Bold, amino acids implicated in putative zinc coordination. The additional cysteine in position 213 is highlighted in blue. Predicted secondary structures of PML B-box-2 are depicted. Arrow, beta-sheet; loop, α1-helix; stars, evolutionary conserved amino acids (bold, identical; star custom, 1/6 variation only). The highly conserved α-helix is boxed in blue. Bottom, PML-RARA mutations from patients with therapy-resistant APL. **B,** Crystal structure of PML B2 monomer shown in a cartoon representation. PML B2 folds around two zinc fingers organized in a cross-brace. The C3H1 zinc coordination leaves the C213 free. Helix α1 (C213 to L218) exposes C213 toward the outside of the structure. Cyan sphere, zinc atoms; blue bold font, C213. **C,** Left, composite omit map contoured at 2 σ of a segment from PML B2 near zinc finger 1 at 2.1 Å. C213 appears as a free cysteine (blue bold font). Right, composite omit map contoured at 2 σ of a segment from PML B2 near zinc finger 2 at 2.1 Å. C227, not D219, coordinates Zn^{2+}. Grey spheres, zinc atoms.

Crystal Structure of PML B2 Box Reveals an α-Helix Exposing C213

B-box domains are found in TRIM proteins and are often involved in protein–protein interaction (31). We identified a highly conserved short sequence encompassing the adjacent cysteines C212/C213 in all PML-like proteins across evolution (Fig. 3A). Interestingly, this stretch of conserved residues exactly corresponds to the hotspot mutations of PML-RARA or PML in patients with therapy-resistant APL (35–38).

Despite numerous attempts, no PML B2 crystal structure has been reported to date. We fused MBP to PML B2 to produce a soluble fusion protein from bacteria and obtain a crystal structure at 2.1 Å resolution (Fig. 3B; Supplementary Fig. S2A). In this structure, the B2 domain adopted a typical B-box–type zinc finger fold, where C3H1 residues coordinated two zinc atoms in a cross-braced conformation and with a conserved β1–β2–α1 arrangement (Fig. 3B and C). Analysis of the crystal packing showed that B2 was sandwiched between two MBP molecules. Indeed, B2 β1 formed an antiparallel β sheet with MBP β8 through main chain hydrogen bonds, while B2 α1 packed against a hydrophobic patch in the neighboring MBPs (Supplementary Fig. S2A–S2C). Structure alignment demonstrated that PML B2 was similar to other TRIM family B2 domains, such as TRIM5 or TRIM28, although PML B2 appears to be more flexible with longer loops (Supplementary Fig. S2D–S2G; refs. 39, 40). In the first zinc finger, zinc coordination involved C212, but importantly, not C213, which was positioned at the edge of the α1-helix pointing out of the overall B2 structure (Fig. 3B and C). Remarkably, this helix corresponds to the evolutionary conserved primary sequence identified above (Fig. 3A; Supplementary Fig. S2D and S2F). In the second zinc finger, the zinc was coordinated by C227 instead of the Alphafold-predicted D219 (Fig. 3B; Supplementary Fig. S2D and S2E). Note that C227 is not conserved in TRIM5 or TRIM28 B2 nor are the residues from the conserved α-helix (Supplementary Fig. S2D–S2G). The residues equivalent to PML C227-surrounding sequence in TRIM5 and TRIM28 form a β3 strand that does not coordinate zinc (Supplementary Fig. S2D, S2F, and S2G). Altogether, we have unraveled the PML B2 structure, highlighting an α-helix that positions outwards the free C213 that is key to NB assembly.

PML B2 α1-Helix and C213 Drive NB Assembly and Dynamics

To determine the respective roles of PML B2 zinc fingers and the C213-containing helix in NB assembly, we engineered mutations disrupting zinc coordination (C189S or C212S) or point mutations on the α1-helix (C213S or L218G) and stably expressed these GFP-tagged PML mutants in *Pml*^{KO} MEFs. All these PML mutants exhibited a sharply increased nuclear diffuse fraction with only one to three unusually large bodies, implying that this α1-helix and C213 play key roles in NB formation (Fig. 4A; Supplementary Fig. S3A).

FRAP analysis showed a slight increase in the GFP-PML^{C189S}, GFP-PML^{C212S}, or GFP-PML^{C215S} body assembly dynamics, with similar immobile fractions when compared with WT PML (Fig. 4B and C; Supplementary Fig. S3B). In contrast, C213S or L218G mutations drastically increased the dynamics of PML NB assembly, with a drop of the half recovery time from 3.2 minutes to 0.6 or 0.8 minutes, respectively. Moreover, we observed a complete recovery of the photobleached C213S and L218G PML proteins at the remaining body, pointing to a fully liquid compartment. Thus, the α1-helix, including C213, dictates PML dynamics and NB assembly. The crystal structure of MBP-PML B2 with C213A and A216V double mutation (A216V being the hotspot mutation driving ATO resistance; refs. 35, 36) was very similar to that of WT B2, with a size exclusion chromatography with multi-angle light scattering (RMSD) of 0.26 Å over 42 Cα atoms (Fig. 4D; Supplementary Fig. S3C). This supports the idea that the effects of these α1-helix mutations on PML NB assembly dynamics were not due to B2 folding alterations, but rather to loss of its biochemical interactions. Overall, while the zinc fingers contribute to the overall domain structure, the conserved α1-helix is crucial for PML NB assembly and dynamics.

α-Helix Mediated Hydrophobic B2 Trimerization Is Key for NB Dynamics

TRIM5α B2 was proposed to trimerize through a specific α-helix around a tryptophan core *in vitro* (39). We thus looked whether PML B2 monomers could self-assemble into a trimer through Alphafold2 molecular modeling (Fig. 5A and B). In the model, the trimer is predicted to be driven by α1-helix–mediated interactions, involving hydrophobic interfaces and in particular, I202, C213, A216, L217, and L218 (Fig. 5A). More specifically, L217 is predicted to play a central role through its two methyl groups, each bridging two other PML B2 monomer through their own L217, as well as with one I202 on β1 (Fig. 5B). Interestingly, L218 could also interact with I202 of another PML B2, further securing this B2 complex (Fig. 5B). Supporting B2 trimerization *in vitro* size exclusion chromatography with multi-angle light scattering (SEC-MALS) analysis revealed three forms of purified MBP-B2 with molecular weights corresponding to monomer, dimer and, critically, abundant trimer (Fig. 5C).

To interrogate the relevance of this model *in cellulo*, we generated point mutations of these potentially interfacing residues. When analyzed by immunofluorescence, L217G substitution had the most drastic effect, completely blocking PML NB assembly (Fig. 5D, quantification in Supplementary Fig. S3A). GFP-PML^{I202A} or GFP-PML^{L218G} localization were diffuse in the majority of cells and formed one or two bodies in the remaining ones. A similar defect in NB assembly was observed with the A216V patient-derived mutation (35–37), consistent with our model predicting a constraint environment due to the short distance between A216 and L217 side chain within the trimer (Fig. 5B and D). In contrast, the A216G mutation had only minor effects, increasing the diffuse PML fraction, consistent with its predicted modest impairment of trimerization. When analyzed in FRAP, PML^{I202A}, PML^{A216V}, or PML^{L218G}, all exhibited highly dynamic exchange with liquid-like behaviors (Fig. 4B; Supplementary Fig. S3B). Conversely, increasing hydrophobicity by substituting leucine to residues with aromatic group at position 218 led to the formation of filaments, on which PML exchange was poorly dynamic (Fig. 5E; Supplementary Fig. S3D and S3E). Thus, the α1-helix–mediated hydrophobic interactions between PML monomers through I202, L217, and L218 regulate PML assembly ranging from large liquid-like bodies to standard PML NBs, up to gel-like PML filaments.

Arsenic Docks on a C213 Tri-Cysteine Pocket of B2 Trimers to Drive Gel-Like Transition

In APL, ATO, and other therapeutic arsenic derivatives provide trivalent arsenic (As(III) oxidation state) at physiologic pH and *in vivo*. As(III) can form stable complexes with thiol groups through covalent binding to sulfur and may form complex with three glutathiones in solution (30). Critically, the key C213 residues are organized in a triad positioned at the center of the PML B2 helix trimer (Fig. 6A; Supplementary Fig. S4A and S4B), in an enzymatic active center-like configuration. This triad is present

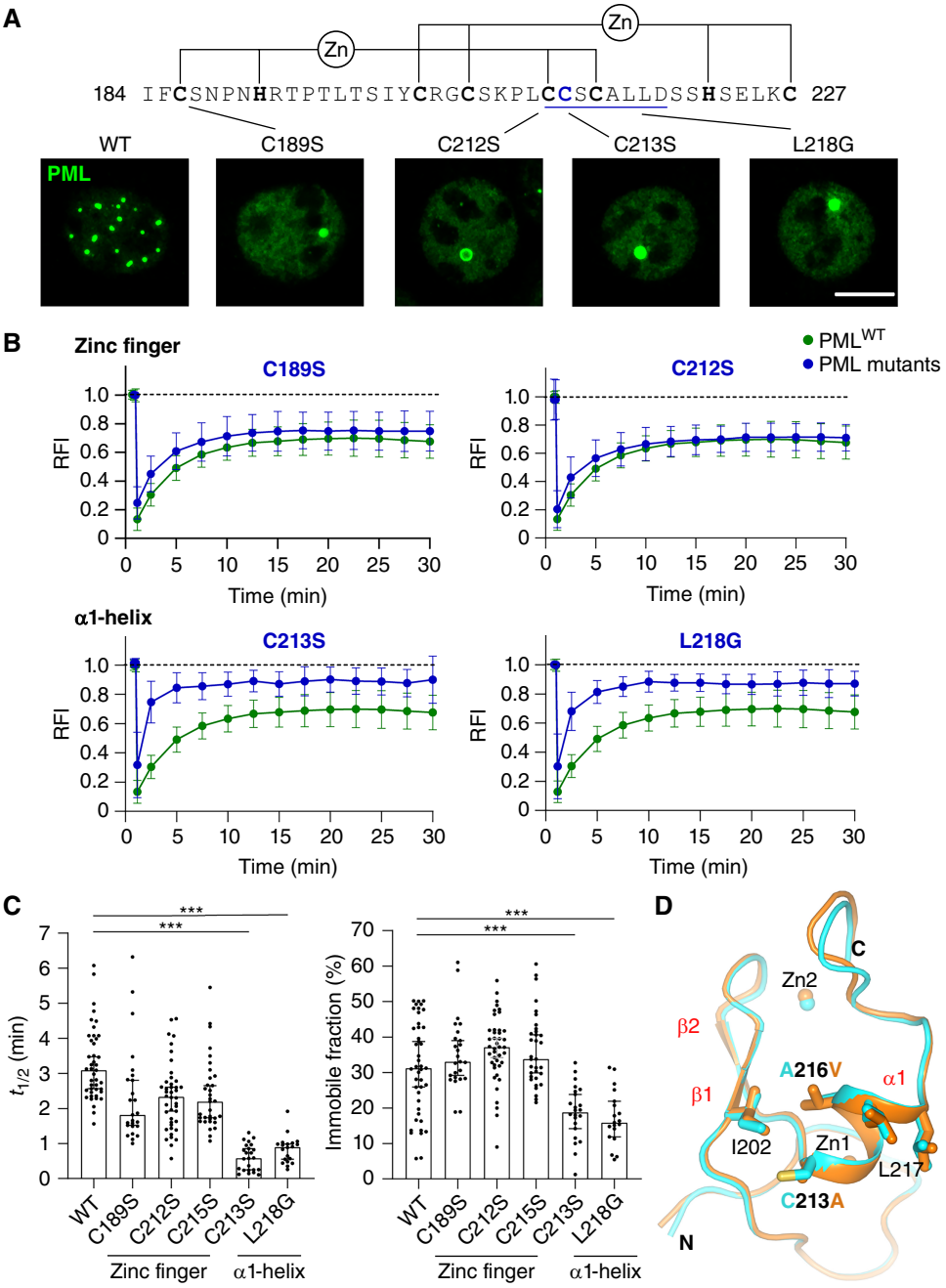

Figure 4. PML B2 α1-helix controls PML assembly and dynamics. **A,** Representative PML NB formation in MEFs expressing PML B2 mutants in Zn^{2+}-coordinating cysteines or α1-helix (underlined in blue) residues. Scale bar, 5 μm. **B,** FRAP analyses of GFP-PML dynamics at NBs in WT- or mutant-expressing MEFs. Mean value ± SD. RFI, Relative fluorescence intensity. NBs assessed PML^{WT} ($n = 36$), PML^{C189S} ($n = 25$), PML^{C212S} ($n = 42$), PML^{C213S} ($n = 24$), PML^{L218G} ($n = 20$), from at least five independent experiments. **C,** Plot representation of **B**, with $t_{1/2}$ (left) and immobile fraction (right) of PML mutants harboring mutations on the α1-helix or zinc finger. Each dot represents an individual NB. Median ± 95% confidence interval, statistical significance by comparison with GFP-PML^{WT}, Kruskal–Wallis test. ***, $P \leq 0.001$ are displayed. *P* value for Zn-finger mutants, C189S = 0.0097, C212S = 0.0115, C213S = 0.028. **D,** Superposition of PML B2 crystal structure (cyan) with that of $PML^{C213A/A216V}$ mutant (orange) demonstrates absence of misfolding.

at the opposite end of the assembled helices compared with the sites of L217 interactions (Figs. 5B and 6A). The C213 residues are separated by 3.2 Å, fitting with an ideal arsenic docking that would lead to an interacting distance of 2.7 Å between arsenic and the sulfur atoms (Fig. 6A; Supplementary Fig. S4A and S4B). We thus hypothesized that ATO could trigger gel-like transition of PML NBs by targeting this triad of C213 residues within the B2 trimer. We first tested whether the effect of ATO on PML NBs depends on arsenic valency. We used monomethyl arsenic (MMA), which can only bind two cysteines, as well as antimony (Sb) trioxide (STO) that releases trivalent Sb, the closest chemical to As(III). In contrast to ATO, MMA has no effect on the dynamics of PML NB assembly (Fig. 6B; ref. 41). Conversely, STO had very similar effects to ATO, decreasing the PML diffuse fraction, turning PML NBs in gel-like string bodies (Fig. 6B; Supplementary Fig. S4C), and subsequently increasing PML sumoylation (Supplementary Fig. S4D; ref. 42).

For B2 mutants of zinc finger 1 formation (C212S, C189S), or mutants impairing helix-driven trimerization, as well as for C213S, PML nuclear distribution was unaffected by ATO treatment (Fig. 6C). ATO could not drive phase transition of C213S or helix trimer mutant-forming bodies, as supported by FRAP analyses (Fig. 6D; Supplementary Fig. S4E). In contrast, A216G mutation only marginally affected ATO response of PML, as expected from our model (Fig. 6C and D). ReAsH, an arsenic derivative that fluoresces when bound to proteins, labeled the

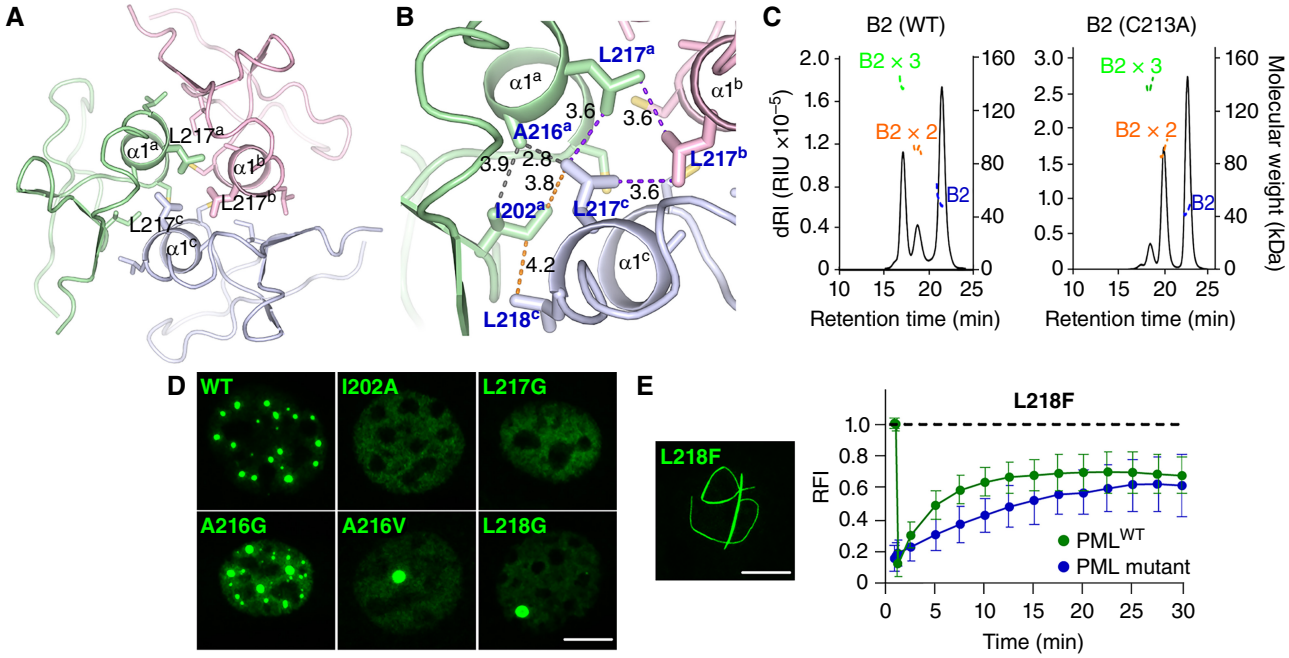

Figure 5. PML B2 mediates PML trimerization and is required for biological functions. **A,** Modeling of a PML B2 trimer. B2 monomers are colored in green, gray, and pink. Exponents refer to affiliation to a specific monomer. **B,** Close-up view of the PML B2 trimer model depicting hydrophobic interactions between the α1-helices. Residues involved in these hydrophobic interactions are shown in blue, linked by dashed lines. Distance between these key hydrophobic residues are in Å. **C,** SEC-MALs analysis showing a mix of monomeric, dimeric, and trimeric PML B2 (left) (dRI:differential refractive index, RIU:refractive index unit). The C213A mutant shifts toward monomeric and dimeric states (right). MBP-B2 molecular weight: 46.2 kDa. **D,** Representative PML NB formation in PML B2 mutants predicted to impair trimerization expressed in MEFs. Scale bar, 5 μm. **E,** GFP-PML^{L218F} yields filaments (left). Scale bar, 5 μm. FRAP analysis of the exchange rates of GFP-PML^{L218F} mutant compared with GFP-PML^{WT} (right). Mean value ± SD. NBs assessed PML^{WT} ($n = 36$) and PML^{L218F} ($n = 24$), from at least five independent experiments. RFI, Relative fluorescence intensity.

GFP-PML^{WT} shell and triggered gel-like transition of PML NBs, similar to ATO (Fig. 6E; ref. 8). In contrast, the shell of the body formed by PML^{C213S} could not bind ReAsH. Rather, ReAsH accumulated within the NB inner core, an unexpected observation that deserves further studies. Similarly, PML^{L218G} failed to bind ReAsH, stressing the fact that efficient arsenic binding depends on both C213 and α1-helix trimerization. Finally, the effect of ATO on PML NBs after 30-minute exposure was not reversed by washout experiments after removing ATO, suggestive for covalent binding (Supplementary Fig. S4F). Altogether, our findings imply that As(III) requires prior B2 helix trimerization to directly and irreversibly targets C213 and trigger gel-like transition.

While mutations of C213 removing thiol group (C213S or C213A) and increasing steric hindrance (C213L or C213F) all disrupted basal PML NB assembly, replacing C213 by valine unexpectedly fully rescued the basal NB formation and normal dynamics (Fig. 6D and F). These data suggest that the branched methyl groups of three valines can maintain hydrophobic interactions within the center of the B2 trimer, somehow similar to L217 on the other side of the helix. Strikingly, both PML C213V localization and dynamics were insensitive to ATO, implying that the sensor function was lost (Fig. 6C and D). Accordingly, alkylation by NEM, which disrupted WT NBs, had no effect on PML^{C213V} NBs (Figs. 2A and 6G), stressing the unique features of this cysteine residue. Altogether, this suggests that, within the B2 domain, C213 thiol modification controls PML NB assembly dynamics.

Figure 6. ATO binding to B2 trimer is responsible for ATO-induced phase transition. **A,** Modeling of PML B2 trimer around an arsenic atom. The key C213 residues are indicated in blue and the arsenic atom is shown as an orange sphere. The predicted distance between the arsenic atom and C213 represented by the dashed line is around 2.7 Å. **B,** FRAP analyses of GFP-PML^{WT} dynamics at NBs in untreated cells or cells treated with trivalent metalloid oxides: ATO (1 μmol/L, 30 minutes) or STO (1 μmol/L, 30 minutes) or divalent arsenic (MMA, 1 μmol/L, 30 minutes). Mean value ± SD, assessed NBs control (Ctrl; $n = 36$), MMA ($n = 21$), ATO ($n = 28$), STO ($n = 33$), from at least five independent experiments. RFI, relative fluorescence intensity. **C,** Representative confocal analyses of PML NB formation in *Pml*^{KO} MEFs stably expressing GFP-PML B2 mutants, ± ATO (1 μmol/L, 1 hour). Scale bar, 5 μm. **D,** FRAP analyses of GFP-PML mutant–expressing MEFs treated or not with ATO (1 μmol/L, 30 minutes). Mean value ± SD. NBs assessed PML^{C212S} Ctrl ($n = 42$), PML^{C212S} ATO ($n = 28$), PML^{C213S} Ctrl ($n = 24$), PML^{C213S} ATO ($n = 27$), PML^{L218G} Ctrl ($n = 20$), PML^{L218G} ATO ($n = 26$), PML^{A216G} Ctrl ($n = 40$), PML^{A216G} ATO ($n = 28$), PML^{A216V} Ctrl ($n = 43$), PML^{A216V} ATO ($n = 43$), PML^{C213V} Ctrl ($n = 32$), PML^{C213V} ATO ($n = 31$), from at least five independent experiments. **E,** Representative images of red fluorescent arsenic (ReAsH) localization to NBs in GFP-PML^{WT} or mutant MEFs. Scale bar, 1 μm. **F,** Representative PML NB formation in PML C213 mutant–expressing MEFs. Scale bar, 5 μm. **G,** Confocal analysis of PML NB formation following cysteine alkylation with NEM (10 μmol/L, 1 hour) in GFP-PML^{WT}- or PML^{C213V} -expressing MEFs. Scale bar, 5 μm. **H,** Western blot analysis of basal PML sumoylation in GFP-PML^{WT}- or mutant-expressing MEFs (arrowheads highlight different sumoylation levels of PML mutants). **I,** Western blot analysis of PML sumoylation in GFP-PML^{WT} or mutant MEFs treated or not with ATO (1 μmol/L, 1 hour). **J,** Confocal analysis of PML and Sp100 localization in GFP-PML^{WT}- or C213 mutant–expressing MEFs treated or not with ATO (1 μmol/L, 1 hour). Scale bar, 5 μm. **K,** Pulldown of HIS_{10}-$SUMO_2$ conjugates from *Pml*^{WT} or *Pml*^{L222G} mESCs treated or not with ATO (1 μmol/L, 30 minutes). ATO-treated nontransduced *Pml*^{WT} mESCs are shown as controls. Western blot with anti-SUMO2/3 (left), anti-mPML (right, top), or anti-KAP1 antibodies (right, bottom). Sumoylated species are indicated. Representative data of $n = 3$ independent experiments.

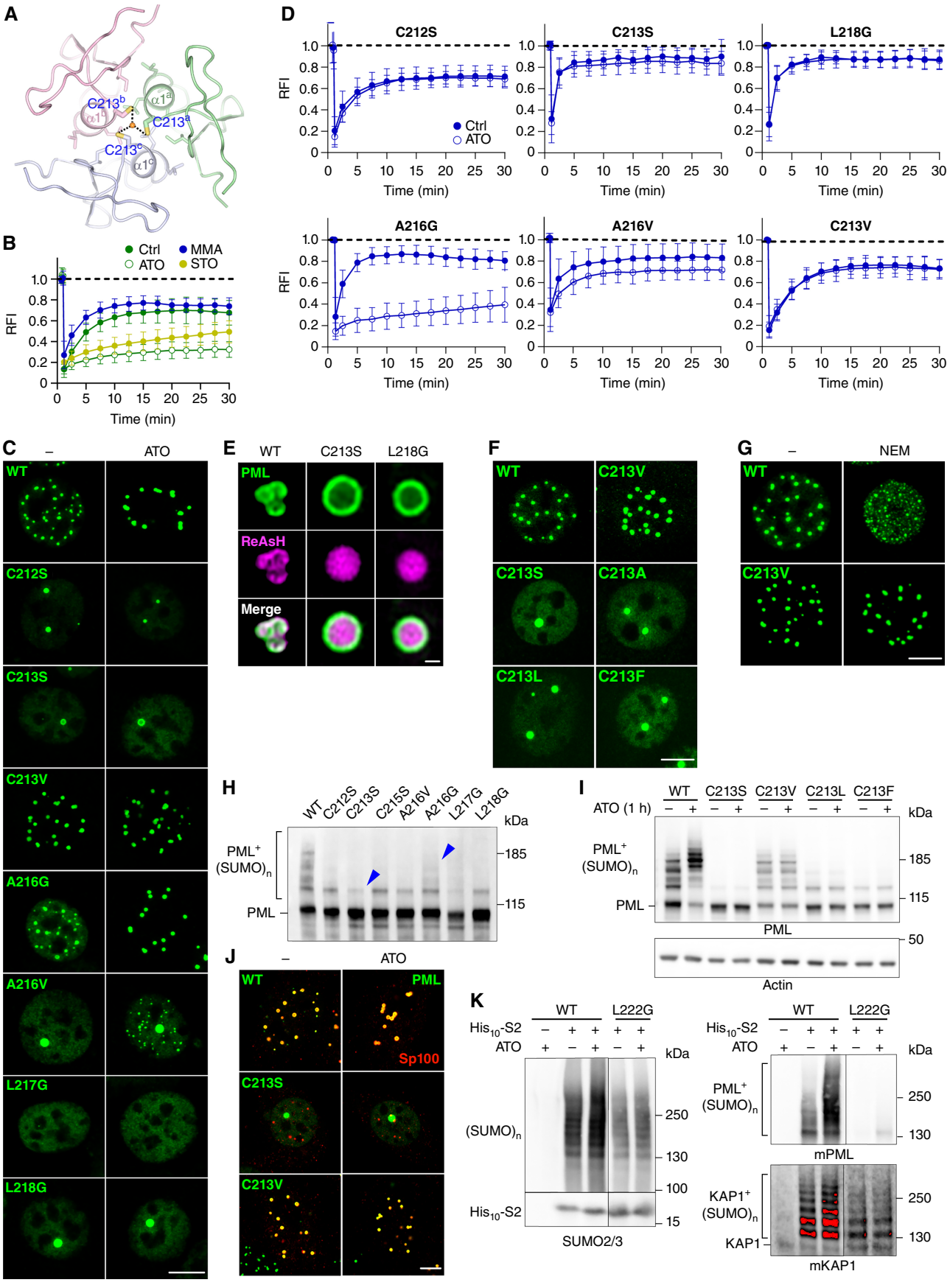

Basal PML sumoylation was severely impaired in all mutants predicted to destabilize the B2 trimer and alter NB formation (Fig. 6H and I). In contrast, basal PML^{C213V} sumoylation was normal or even enhanced (Fig. 6I), while critically, sumoylation of PML^{C213V} was ATO-insensitive (Fig. 6I; Supplementary Fig. S4G and S4H). As expected, all B2 trimer and other C213 mutants were resistant to ATO-enhanced sumoylation. PML sumoylation of K160 drives partner recruitment (18, 43). Accordingly, PML^{C213V} efficiently recruited partner proteins, such as Sp100 (Fig. 6J) and the RNF4 SUMO-dependent ubiquitin ligase (Supplementary Fig. S4I), while PML^{C213S} did not. As expected, in contrast to PML, ATO did not further promote recruitment of partners into C213V bodies (Fig. 6J). Accordingly, all B2 mutants were resistant to ATO-induced SUMO-triggered degradation (Fig. 6I; Supplementary Fig. S4G and S4H). Thus, C213-mediated trimerization controls PML sumoylation and partner recruitment.

PML NBs couple oxidative stress to control of partner sumoylation through recruitment of UBC9 (18, 21). We questioned whether impeding α1-helix-mediated B2 trimerization would affect partner biochemical modifications. We generated a *Pml*^{L222G} mESC line (corresponding to L218G in human PML, forming liquid-like bodies), stably expressed His$_{10}$-SUMO2 and we purified SUMO2 conjugates before or after ATO exposure. As we previously described (21), ATO enhanced global sumoylation, as well as that of endogenous mouse PML (mPML) and KAP1 (Fig. 6K). None of these were observed in *Pml*^{L222G} mESCs (Fig. 6K; Supplementary Fig. S4J). Thus, α1 helix-mediated B2 trimerization is required for the biochemical function of PML NBs to promote partner sumoylation.

C213 Mediates PML-RARA ATO Sensitivity

We then assessed the role of PML C213 residue in the context of the oncogenic PML-RARA protein, by transducing hematopoietic progenitors [hematopoietic stem and progenitor cells (HSPC)] and MEFs with WT or C213 mutant PML-RARA. We first examined the distribution of human PML-RARA and endogenous mouse Pml proteins by immunofluorescence. As previously shown (27, 44), PML-RARA^{WT} exhibited a microspeckled pattern where it recruited endogenous mPML. In contrast, PML-RARA^{C213S} was diffuse in the nucleus, consistent with C213 role in PML-RARA self-assembly, but endogenous mPML NB formation was unaffected in both MEFs (Fig. 7A) and HSPCs (Supplementary Fig. S5A). PML-RARA^{C213V} formed numerous small microdots and also disrupted endogenous mPML localization, similar to PML-RARA^{WT}. Thus, C213 controls the efficiency of homo- and hetero-interactions between PML-RARA and Pml within microspeckles. In ATO-treated primary progenitors or MEFs, PML-RARA and mPML progressively reassembled into NBs (Fig. 7A; Supplementary Fig. S5A). In sharp contrast, PML-RARA^{C213S} did not respond to ATO, while endogenous mPML aggregated into fewer NBs (Fig. 7A; Supplementary Fig. S5A). Finally, PML-RARA^{C213V}-expressing cells had a mixed phenotype, with ATO-aggregated endogenous mPML NBs, particularly in progenitors that express high levels of mPML proteins, but with unresponsive PML-RARA micro-speckles. We then examined the effects of ATO on PML-RARA sumoylation/degradation (45). In the context of the oncogenic protein, C213S precluded basal PML-RARA sumoylation, while PML-RARA^{WT} or PML-RARA^{C213V} were both efficiently sumoylated in the basal state (Fig. 7B). Importantly, the two C213 mutants were completely resistant to ATO-triggered hyper-sumoylation and degradation (Fig. 7B quantification in Supplementary Fig. S5B), explaining the remaining PML-RARA^{C213V} microspeckles (Fig. 7A; Supplementary Fig. S5A). In FRAP analyses performed either in *Pml*^{WT} (Supplementary Fig. S5C and S5D) or *Pml*^{KO} MEFs (Fig. 7C), GFP-PML-RARA^{C213V} exhibited a reduced basal assembly dynamics compared with that PML-RARA microdots. This mutation blocked ATO-driven gel-like transition, consistent with PML-RARA^{C213V} inability to bind arsenic. Altogether, these data demonstrate the key role of C213 in ATO-targeted effects on PML and PML-RARA. Interestingly, dynamics of GFP-PML-RARA were distinct in *Pml*^{WT} or -*Pml*^{KO} background (Fig. 7C; Supplementary Fig. S5C), supporting the idea that PML reduces PML-RARA assembly dynamics and could contribute to its ATO sensitivity.

B2 Trimer and C213 Control Oxidative Stress Responses

The role of PML is likely much broader than being just an arsenic binder and PML was repeatedly linked to oxidative stress control (46–49). To question any contribution of the C213 triad in oxidative stress sensing, we compared the effects of ROS on PML NB assembly dynamics in PML^{WT}- and PML^{C213V}-expressing MEFs. Depending on the dose, H_2O_2 increased or decreased PML dynamics assessed by FRAP (Fig. 7D). Remarkably, PML^{C213V} was completely insensitive to H_2O_2 (Fig. 7E), suggesting that C213 modification by ROS regulates NB dynamics and could play an important role in oxidative stress sensing.

Figure 7. PML-RARA ATO sensitivity requires C213 and B2 controls *in vivo* responses to ROS. **A,** Confocal analysis of *Pml*^{WT} MEFs stably expressing human GFP-PML-RARA^{WT} or its B2 mutants treated or not with ATO (1 μmol/L, 6 hours). Scale bar, 5 μm. Different display settings for each genotype. **B,** Western blot analysis of PML-RARA sumoylation in Lin$^-$ hematopoietic progenitors expressing PML-RARA or the indicated mutants, treated or not with ATO (1 μmol/L, 1 hour). Representative data from three independent experiments. **C,** FRAP analysis of GFP-PML-RARA dynamics at NBs in GFP-PML-RARA^{WT}- or GFP-PML-RARA^{C213V}–expressing *Pml*^{KO} MEFs treated or not with ATO (1 μmol/L, 30 minutes). Mean value ± SD. NBs assessed PML-RARA^{WT} ($n = 20$), PML-RARA^{WT}+ATO ($n = 37$), PML-RARA^{C213V} ($n = 42$), PML-RARA^{C213V}+ATO ($n = 25$), from at least five independent experiments. RFI, relative fluorescence intensity. **D,** FRAP analysis of GFP-PML^{WT} dynamics at NBs in MEFs treated or not with H_2O_2 (30 minutes). Mean value ± SD. NBs assessed PML ($n = 35$), H_2O_2 100 μmol/L ($n = 27$), H_2O_2 500 μmol/L ($n = 32$), from at least five independent experiments. Ctrl, control. **E,** Same as **D** with GFP-PML^{C213V}. Mean value ± SD. NBs assessed PML^{C213V} ($n = 32$), H_2O_2 100 μmol/L ($n = 24$), H_2O_2 500 μmol/L ($n = 22$), from at least five independent experiments. **F,** Box plot representing γH2AX dots counts assessed by immunofluorescence on liver tissues from three untreated mice. *Pml*^{WT} ($n = 633$), *Pml*^{KO} ($n = 527$), *Pml*^{A220V} ($n = 333$). ***, $P \leq 0.001$, unpaired *t* test. **G,** Gene-set enrichment analysis (GSEA) of differentially expressed genes from liver samples from untreated *Pml*^{WT} or *Pml*^{A220V} (equivalent of human *PML*^{A216V}) mice. Key pathways are boxed. Livers from $n = 3$ *Pml* or *Pml*^{A220V} mice. **H,** GSEA of differentially expressed genes in liver samples from *Pml*^{KO} or *Pml*^{A220V} in comparison to *Pml*^{WT} after an 18-hour CCl_4 treatment. Key pathways are boxed. Livers from $n = 3$ mice of each genotype. **I,** Liver fibrosis following a 5-week CCl_4 treatment detected by Picrosirius Red staining (left). Quantification of the fibrotic areas (right). Livers from $n = 7$ *Pml*, *Pml*^{KO}, or *Pml*^{A220V} mice. Scale bar, 400 μm. **, $P \leq 0.01$, Mann–Whitney test. **J,** Model of PML NB liquid to gel-like transition controlled by the B2 α1 helix exposing C213 and hijacked by ATO. Hydrophobic-mediated trimerization of PML B2 (gray disk), regroups the three C213 in the center of the structure. The latter is impaired in α-helix mutants. In the physiologic states, this C213 triad behaves as a rheostat depending on their oxidation state (asterisks), fine-tuning the interactions within the trimer (light and dark gray disk). Arsenic binding crosslinks these cysteines, hijacking the ROS-rheostat to yield polymerization-induced gel-like transition.

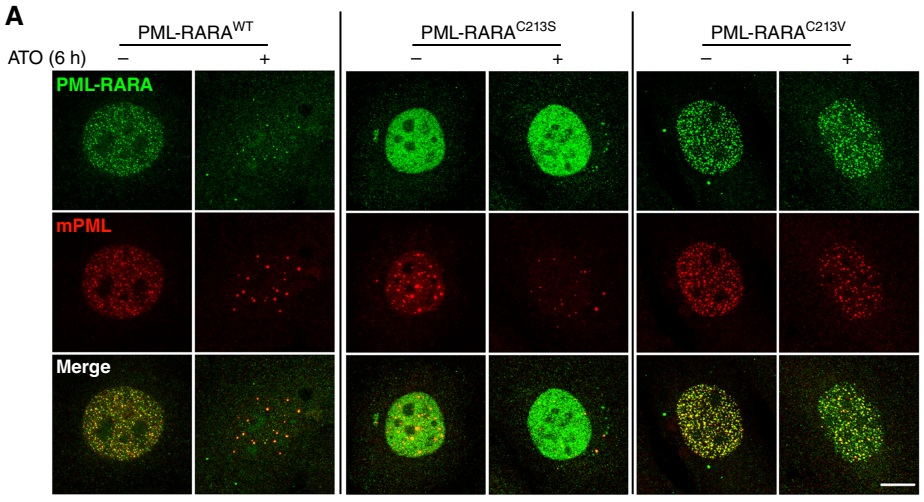

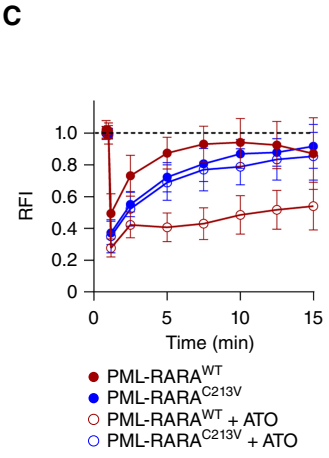

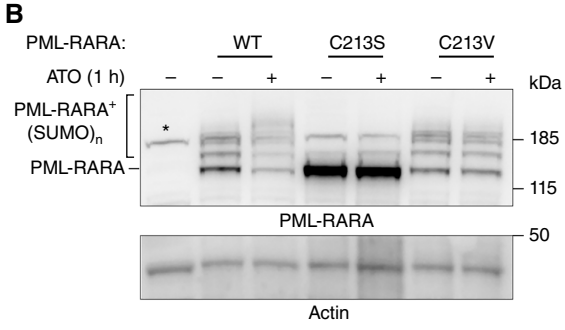

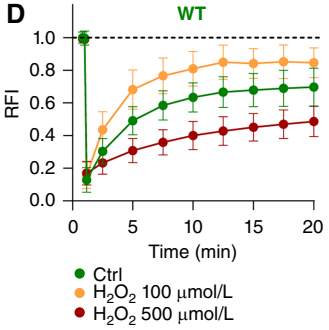

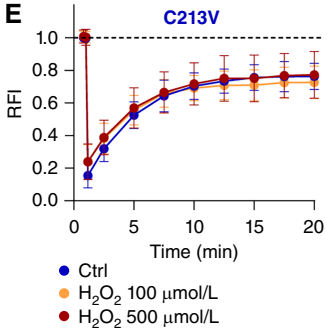

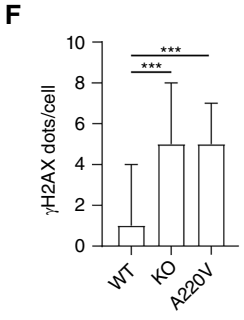

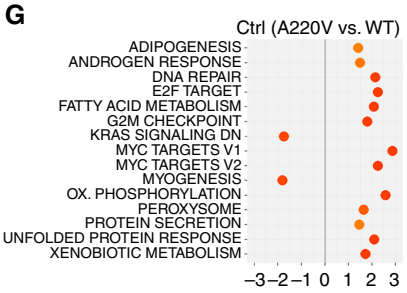

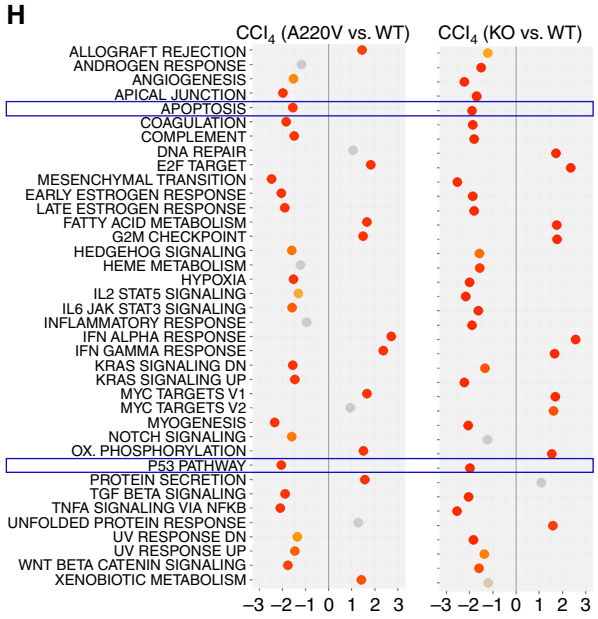

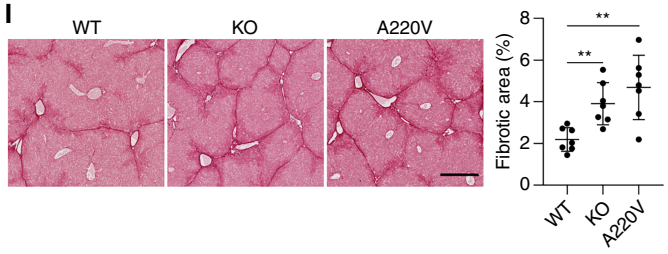

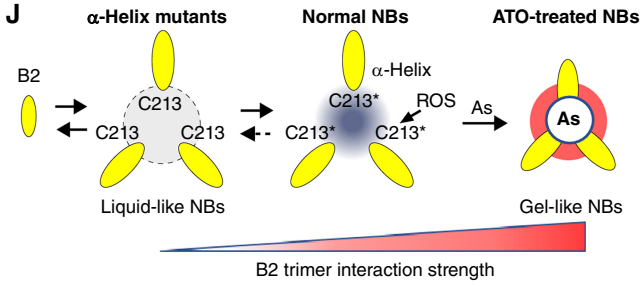

PML is involved in oxidative stress responses (50, 51), notably in hepatocytes (46). To explore any role of B2 trimerization, we engineered a *Pml*^{A220V} knock-in mice (corresponding to the A216V hotspot mutation in the human sequence). Similar to *Pml*^{KO} mice, these animals did not exhibit obvious phenotypes and were fertile. As for stably expressed PML^{A216V} mutant in MEFs (Fig. 5D), rare mPML^{A220V} NBs were observed in hepatocytes and the mutant protein did not undergo detectable sumoylation (Supplementary Fig. S5E). Hepatocytes from *Pml*^{A220V} or *Pml*^{KO} animal exhibited an increased number of γH2AX foci (Fig. 7F), which could reflect basal oxidative stress (46) or defects in DNA repair (52). Transcriptomic studies and gene-set enrichment analysis (GSEA) analyses comparing basal gene expression in the livers of *Pml*^{A220V} and WT animals revealed major differences (including stress signatures, Fig. 7G), many of which were shared with *Pml*^{KO} animals (Supplementary Fig. S5F). Thus, B2 trimer formation has important consequences in physiologic conditions.

We then subjected WT, *Pml*^{A220V}, and *Pml*^{KO} animals to CCl_4, a classic trigger of oxidative stress, ultimately resulting in fibrotic scars, which are limited by senescence activation (53). We first examined acute response by performing transcriptomic studies of livers 18 hours postinjection. Remarkably, differentially regulated pathways compared with WT animals were virtually identical between *Pml*^{A220V} and *Pml*^{KO} ones (Fig. 7H), highlighting defects in multiple pathways, including p53, E2F, G2M checkpoint, fatty acid, hypoxia, IFNs, Myc, TNFα, or TGFB. They are functionally related to processes regulated by PML, such as apoptosis and senescence, cell growth, metabolism, oxidative stress response, as well as inflammatory processes (1, 2, 50). When we examined liver fibrosis after 5 weeks of treatment, increased fibrosis was noted upon Picrosirius red staining in *Pml*^{A220V} and *Pml*^{KO} animals when compared with WT animals (Fig. 7I), as expected from impaired P53 activation and senescence (53).

Altogether our findings support that B2 helix–positioned C213 triads act as rheostats controlling PML NB assembly dynamics, liquid- to gel-like properties, and sumoylation, depending on C213 oxidation states (Fig. 7J). This rheostat controls physiologic functions of PML for basal homeostasis and stress adaptation. As(III) highjacks this sensor, turning reversible interactions into high-affinity ones, ultimately driving PML-RARA sumoylation/degradation and yielding APL cure.

DISCUSSION

In this study, based on the first determination of PML B2-box crystal structure, we unravel the PML/arsenic interplay on a cysteine trio within a B2 trimer, driving a polymerization-like process of PML NB assembly.

Despite repeated claims, there was little available experimental evidence that PML undergoes phase separation. Here, we show that PML can demix from the nucleoplasm, forming bodies as a result of a dynamic process of PML exchange between condense and diffuse fractions, with viscosity similar to other LLPS-driven NBs. PML NB biogenesis and LLPS were proposed to rely on SUMOs and SUMO-interacting motifs (17, 54). Yet, PML mutants on sumoylation sites can nevertheless demix into few bodies, underscoring the dispensable nature of sumoylation for PML condensation (18, 19). Our FRAP data unravels that the typical PML NB assembly dynamics is the result of complex PML self-interactions requiring B2 trimers rather than a simple multi-SUMO/SIM–driven LLPS. PML crystal structure and B2 trimer model resembles that of TRIM5α (39), with PML-specific tunable central cysteine residues that set PML NB assembly dynamics. Liquid-like bodies are defective for PML and partner sumoylation, while ATO-induced gel-like condensates promote both of them. This interplay thus unraveles tight links between NB biochemical activity and B2-controled PML NB dynamics.

Arsenic may bind three adjacent cysteines on the same polypeptide (55, 56). Here, arsenic binding is achieved through a trio of C213 residues from distinct B2 polypeptides, locking a polymeric-like PML complex and driving gel-like transition. *In vivo*, interfering with C213 positioning, with the mouse equivalent of the A216V mutation, induced basal and stress-responsive transcriptional changes similar to those observed in *Pml*^{KO} cells (47). These included defects in p53, E2F, fatty acid metabolism, hypoxia, Myc, TNFα, or TGFB (Fig. 7H), many of which are directly implicated in oxidative stress response and altered in cancers. Thus, in physiologic conditions, the oxidation status of the sulfur atoms of C213 trio could be the rheostat of NB biogenesis, accounting for their oxidative stress sensitivity (46, 48, 51). The biochemical nature of oxidation status changes in the C213 triad remains to be investigated. Distinct from C213, C389-mediated oxidation or disulfide formation may be involved in other functions (33), such as ROS buffering within NBs (21).

ATO-driven APL remission requires PML-RARA degradation and subsequent PML NB reformation (3, 57). PML-RARA^{C213S} lost the ability to form microspeckles and delocalize endogenous mouse PML. In this setting, mPML localization was normal and remained fully ATO sensitive. A similar situation may be observed during clinical resistance observed in patients with PML-RARA B2-mutated APL (36, 37). Thus, although ATO-induced NB restoration is required in murine APL models (57), it may be insufficient on its own to initiate response, without concomitant degradation of PML-RARA and the resulting clearance of master genes promoters (58).

Identification of the 3D catalytic–like site controlling NB assembly could allow the design of novel arsenic-like molecules to enhance or impede NB formation. These could be of high value for PML NB–targeted therapies (59), or conversely, in cancers where PML is an important survival factor (60, 61). Overall, our results elucidate the long-standing question of ATO targeting of PML (62, 63) and unravel novel basic regulatory mechanisms that are likely to be important in other physiopathologic settings.

METHODS

Sequence Analysis, Cloning, and Constructs

Human PML B2 amino acid sequence was extracted from the NCBI databank (NP_150241.2) and compared with the following sequences: *Macaca mulatta* (NP_001035899.1), *Mus musculus* (NP_835188.2), *Molossus molossus* (XP_036113734.1), *Gallus gallus* (XP_004943755.1), *Chrysemys picta bellii* (XP_042707508.1). Amino acid conservation was assessed using the ClustalW2 software (64).

PML mutations were performed in pMSCVpuro-HA-PMLIII or pMSCVpuro-GFP-PMLIII using the Q5 site-directed mutagenesis kit (NEB; catalog no. E0554S) according to the manufacturer's protocol and controlled by sequencing (Eurofins Genomics). PML-RARA was cloned into pMSCVpuro (*Sfi*I/*Age*I) from pMSCVpuro-GFP-PMLIII and pMSCV-PML-RARA-neo. PML-RARA B2 mutants were generated using *Avr*II/*Sfi*I restriction fragments from pMSCVpuro-GFP-PMLIII mutants. Restriction enzymes and T4 DNA ligase were purchased from NEB. Additional primer sequences used for site-directed mutagenesis can be found in Supplementary Table S1.

Cell Culture and Cell Treatments

All reagents and cell sources are indicated in Supplementary Tables S2 and S3. Large T-transformed Pml^{KO} MEF cells (our laboratory; ref. 46), HEK293T (Platinum-E from Catherine Lavau, Durham, NC), and HeLa cell lines were maintained in DMEM (Thermo Fisher Scientific, catalog no. 41966029) supplemented with 10% FCS, 50 U/mL penicillin/streptomycin (Thermo Fisher Scientific, catalog no. 10378016), 2 mmol/L glutamine (Thermo Fisher Scientific, catalog no. 25030024), at 37°C with 5% CO_2. Pml^{WT} mESCs were originally obtained from P. Navarro (Pasteur Institute, Paris, France) and cultured in the same culture medium as MEFs, supplemented with 1% nonessential amino acid (Thermo Fisher Scientific, catalog no. 11140050), 1% Glutamax (Thermo Fisher Scientific, catalog no. 35050–038), 1,000 U/mL of recombinant Leukemia Inhibitory Factor (LIF, Sigma-Aldrich, catalog no. ESG1107) and 0.1% β-mercaptoethanol (Merck, catalog no. M6250) on gelatin-coated plates. HSPC isolation, culture, and transformation with PML-RARA were performed as described previously (65). Pml^{KO} MEFs were transduced using retroviruses produced by Platinum-E packaging cells, after transfection with Effectene reagent (Qiagen, catalog no. 301425) with pMSCVpuro-HA-PMLIII or pMSCVpuro-GFP-PMLIII WT or mutants. GFP-positive cells were sorted by flow cytometry (BD FACSAria II, BD Biosciences) or selected using 2 μg/mL puromycin (Sigma-Aldrich, catalog no. P8833). HeLa-PML^{L218Y} cell line was generated by retroviral transduction. pLVX-CMV-GFP-PMLIII L218Y retroviruses were generated by co-transfection into HEK293T cells as above. For colocalization studies between PML and RNF4 or Sp100, Platinum-E cells were transfected with both pMSCVpuro-GFP-PMLIII WT or mutant and pMSCV-Sp100 or pMSCV-Flag-RNF4 and the culture supernatant was used to transduce transformed Pml^{KO} MEFs. All cell lines used were negative for *Mycoplasma* (monthly tested by Eurofins MWG France) and were manipulated separately to avoid any cross contamination during cell passages. The different stable cell lines were at least monthly checked for authentication, based on human or mouse PML expression, sumoylation status, and subcellular distribution by immunofluorescence and Western blot analyses. They were frozen before the third passage and kept for 10 to 20 passages, expect for PML-RARA-transduced MEFs or progenitors were less than five passages. No karyotype was performed, except for knock in mESCs (see below).

Cells were treated with 1 μmol/L As_2O_3 (Sigma-Aldrich, catalog no. 01969), 10 μmol/L N-ethyl-maleimide (Sigma-Aldrich, catalog no. E3876), 100 or 500 μmol/L H_2O_2 (Sigma-Aldrich, catalog no. 516813), 2 μmol/L methylarsonic acid (Greyhouse, catalog no. N-12922), 2 μmol/L cacodylic acid (Sigma-Aldrich, catalog no. C0125), 1 μmol/L antimony oxide (Sigma-Aldrich, catalog no. 637173–100G), or 2 μmol/L ReAsH (Thermo Fisher Scientific, catalog no. T34562).

Western Blot Analysis

Cell extracts were obtained using homemade Laemmli buffer devoid of reducing reagents (200 mmol/L Tris pH 6.8, 8% SDS, 40% glycerol, 0.2% bromophenol blue), supplemented with 20 mmol/L N-ethyl-maleimide (Sigma-Aldrich, catalog no. E3876) for Western blot analysis in nonreducing conditions, or supplemented with 50 mmol/L Tris (2-carboxy-ethyl)-phosphin-HCl (TCEP), or using direct lysis in commercial Laemmli buffer (Sigma-Aldrich, catalog no. S3401). SDS-PAGE analyses were performed with 4%–12% NuPAGE bis-tris gels (Thermo Fisher Scientific, catalog no. NP0336) and immunoblotted on nitrocellulose membranes (BioTrace Pall Laboratory, catalog no. 732–3031), with antibodies: anti-GFP (1/1,000, Roche, catalog no. 11814460001), anti-HA (1/1,000, Covance, catalog no. MMS-101R-1000), anti-Actin (1/1,000; Sigma-Aldrich, catalog no. A2066), homemade anti-hPML. Secondary antibodies from Jackson Immuno-Research: anti-mouse-HRP (1/5,000, catalog no. 115–035–062), anti-Rabbit-HRP (1/5,000, catalog no. 111–035–045). Proteins were detected using SuperSignal West Dura or Femto (Thermo Fisher Scientific, catalog nos. 34076 and 34096), using Vilber Fusion-Fx (Vilber). To avoid nonspecific signals, membranes were not reprobed.

Immunolabeling and Microscopy Analysis

Cells were fixed with 10% formalin (Sigma-Aldrich, catalog no. HT501128) for 15 minutes and permeabilized in PBS 0.5% Triton X-100 (Sigma-Aldrich, catalog no. T9284) for 15 minutes. Incubation with antibodies was performed in PBS 0.5% Triton X-100 for 1 hour. Primary antibodies: anti-GFP (1/1,000, Roche, catalog no. 11814460001), anti-HA (1/1,000, Covance, catalog no. MMS-101R-1000), anti-FLAG (11,000, Sigma-Aldrich, catalog no. F7425), homemade anti-hSP100 antibody, homemade anti-hPML and anti-mPML antibodies, anti-SUMO2/3 (1/500, Cell Signaling Technology, catalog no. 4971P), γH2AX (Cell Signaling Technology, catalog no. 2577S). The following secondary antibodies were used: goat anti-mouse Alexa Fluor 488 (1/500, Jackson Immuno-Research; RRID: AB_2338840), goat anti-mouse rhodamine red-X (1/500, Jackson Immuno-Research; RRID: AB_2338756), goat anti-rabbit Alexa Fluor 488 (1/500, Jackson Immuno-Research; RRID: AB_2338046), goat anti-mouse rhodamine red-X (1/500, Jackson Immuno-Research; RRID: AB_2338022). Secondary goat anti-mouse antibody [STAR RED (1/250, Abberior, catalog no. STRED-1001)] was used for STED analysis. DAPI (1 μg/mL) was from Thermo Fisher Scientific (catalog no. 62248). Image acquisitions were performed using a confocal microscope LSM 980 (Carl Zeiss Micro-Imaging) equipped with an Airyscan 2 super-resolution module using a ×60 oil-immersion objective or by STED microscopy using an Axio Observer 7 (Carl Zeiss Micro-Imaging) equipped with a STEDYCON module (Abberior) using a ×100 oil-immersion objective.

For the study of HeLa PML^{L218Y}, stably expressing cells were fixed with 4% paraformaldehyde and permeabilized with 0.1% Triton X-100. Slides were blocked with 2% BSA in PBS, followed by incubation with anti-Flag antibodies (Sigma-Aldrich, catalog no. F1804) overnight at 4°C. Secondary antibodies (Abbkine, catalog no. A23210) were incubated at room temperature for 4 hours. Slides were mounted using DAPI Fluoromount-G (Southern Biotech, catalog no. 0100–20). The fluorescent signals were visualized under a Zeiss 510 confocal microscope (Carl Zeiss Micro-Imaging).

Live-Cell Imaging and Analysis of PML NBs

All live-cell analyses were performed using glass-bottom culture dishes (IBIDI, catalog no. 81156). For the analysis of NB formation, Pml^{KO} cells were transduced with the culture supernatant of Platinum-E cells transfected two days prior with a pMSCVpuro-GFP-PMLIII vector. Anti-evaporation oil (1 mL) was added on top of the supernatant (IBIDI, catalog no. 50051). The acquisition was performed on an Axio Observer video-microscope (Carl Zeiss Micro-Imaging) equipped with a thermostatic chamber (37°C, 5% CO_2). Laser power and exposure time were set at minimum levels to avoid phototoxicity. Acquisitions were performed every 15 minutes. PML NB formation was tracked in the same cells during the entire experiment.

The quantification of PML NB nucleation/fusion/fission events was performed on Pml^{KO} MEFs stably expressing GFP-PMLIII on a spinning disk confocal microscope (Nikon Eclipse Ti, Nikon) equipped with a Coolsnap HQ2 high-sensitivity camera (Photometrics) and a

thermostatic chamber (37°C, 5% CO_2). Cells were imaged during 2 hours every 30 seconds. Quantification was performed using the FIJI software on maximum Z projections of $n = 37$ cells from four independent experiments. The magnitude of the effective viscosity of the PML NBs was estimated by quantifying the time required for two NBs to relax in a spherical structure during a fusion event, as described before (66). The relaxation time during a fusion event was quantified by measuring the long axis of the two condensates from the beginning of the fusion and was plotted as a function of time for $n = 21$ NBs from three independent experiments. By computing the fusion time as a function of the diameter of the resulting PML bodies (Supplementary Fig. S1B) and by assuming that surface tension drives the fusion process whereas viscosity tends to impede it, we determined that PML bodies have an effective viscosity of about 10^3 Pa·s. Analysis of PML NB distribution was performed on confocal images of fixed cells using the FIJI software.

Analysis by FRAP

FRAP was performed on Pml^{KO} MEFs stably expressing GFP-PML-III, GFP-PML-RARA, or the indicated B2 mutants. One-micron regions of interest (ROI) were used for GFP-PMLIII–expressing cells and 2-μm ROI were used for GFP-PML-RARA. Acquisitions were performed every 10 seconds using a spinning disk confocal microscope (Nikon Eclipse Ti, Nikon) equipped with a Coolsnap HQ2 high-sensitivity camera (Photometrics) and a thermostatic chamber (37°C, 5% CO_2) with a ×60 oil-immersion objective. Three images were taken before photobleaching, 15 iterations were used to bleach the ROI, and fluorescence recovery was followed every 10 seconds for 15 to 30 minutes. On the graphs, only the data points prebleaching, immediately after bleaching, and every 2.5 minutes are shown. Fluorescence recovery was analyzed using the FIJI software. For each studied nucleus, the relative fluorescent intensity (RFI) was calculated as previously described using an ImageJ plugin (67). Background correction was applied at every time point and a double normalization was performed to account for global sample bleaching. We assessed that PML recovery was independent of the size of the bleached area by testing several sizes of photobleached areas, showing that interactions between PML proteins at the shell have a predominant role over free diffusion. Then every RFI curve was fitted to an $y = A^*[1-\exp(-B/t)]$ model where y is the fluorescence intensity, A the plateau of the intensity (mobile fraction), B the time in seconds, and t the half-recovery time ($t_{1/2}$).

Protein Expression and Purification from Bacteria

Escherichia coli Rosetta (DE3) cells (Novagen) were transformed with a pRSFDuet-1 vector (Novagen) containing the DNA sequence of human PML B2 domain fused to an MBP tag. IPTG (0.2 mmol/L) was added into the culture to induce expression of the recombinant proteins at 18°C for 16 hours. Bacteria were harvested by centrifugation (5,000 rpm, 8 minutes), resuspended in a buffer containing 20 mmol/L Tris-HCl pH 8.0, 300 mmol/L NaCl, 5% glycerol, 0.3 mmol/L TCEP, 1 mmol/L phenylmethylsulfonylfluoride and lysed using a cell disruptor (JNBIO). The lysate was loaded onto a preequilibrated amylose resin column (NEB). The column was first washed with 5 column volume of lysis buffer and MBP-B2 protein was eluted with a buffer containing 20 mmol/L Tris-HCl pH 8.0, 300 mmol/L NaCl, 5% glycerol, 0.3 mmol/L TCEP, 10 mmol/L maltose. Proteins were concentrated to 20 mg/mL and purified on a Superdex 200 increase gel filtration column (Cytiva; 20 mmol/L Tris-HCl pH 8.0, 200 mmol/L NaCl, 0.3 mmol/L TCEP). Purified MBP-B2 was concentrated to 15 mg/mL for crystallization.

Crystallization and Structure Determination

Crystals of WT MBP-B2 were grown with 24-well plates using the hanging drop vapor diffusion method by mixing 1.2 μL protein (15 mg/mL) with 1.2 μL crystallization buffer containing 100 mmol/L MES pH 6.5, 250 mmol/L potassium acetate, 22% (w/v) PEG 3350. Crystals grew to full size after incubation at 16°C for 1 week. MBP-B2 C213A and A216V-mutant proteins were crystalized in the same conditions. Before X-ray diffraction, crystals were cryoprotected with the reservoir solution supplemented with 25% glycerol and were flash-cooled into liquid nitrogen. Diffraction data were collected at Beamline station BL19U1 of Shanghai Synchrotron Radiation Facility (SSRF, Shanghai, China), integrated and scaled using XDS and the CCP4 program Pointless and Aimless (68–70). The structure of MBP-B2 was determined by molecular replacement using the MBP structure from PDB 1ANF as an initial searching model with Phaser (71). The structural model was built using Coot (72) and refined using PHENIX (73). The structure of MBP-B2 C213A and A216V was determined using WT MBP-B2 structure as the initial search model. Figures were generated using PyMOL (The PyMOL Molecular Graphics System, Version 2.0 Schrödinger, LLC). The statistics of the data collection and refinement are shown in Supplementary Table S4. The B2 trimer model was generated with Alphafold 2 (74). Relevant crystallographic data collection and refinement statistics are provided in Supplementary Table S4. Experimentally determined 3D structures can be found from the Protein Data Bank (PDB ID: 8J2P and 8J25).

SEC-MALS Analysis

SEC-MALS were performed using a Superdex 200 increase column (Cytiva) combined with multi-angle laser light scattering using a Wyatt HELEOS-II 18-angle photometer coupled to a Wyatt Optilab rEX differential refractometer (Wyatt Technology Corp). Experiments were carried out at room temperature with a protein concentration of 2.0 mg/mL and a flow rate of 0.5 mL/minute in 20 mmol/L Tris-HCl pH 8.0, 200 mmol/L NaCl, 0.3 mmol/L TCEP. The data were analyzed using the ASTRA 6.1 software (Wyatt). The molecular mass was determined across the protein elution peak.

CRISPR/Cas9 Knock-In mESCs and His Pulldown

Pml^{KO} cells were generated as described previously (21). To generate Pml^{L222G} mESCs, gRNA targeting mouse Pml (5′-G· CCG AGG CTG CGC CAA GCC TCT GTG TTG CAC ATG CGC GCT CGG GGA CCG CAA CCA CAG CCA TCT CCA TTG CGA TAT TGG TG·A·G-3′) and recombinant Cas9 protein were synthesized from IDT to form Alt-R CRISPR/Cas9 ribonucleoprotein. mESCs were transiently transfected with Alt-R CRISPR/Cas9 ribonucleoprotein by using Amaxa mouse ES cell Nucleofector kit (Lonza, catalog no. VPH-1001) and program number A-013 from the nucleofector 2b device (Lonza). After three days, 200 mESCs were spread on 150-mm cell culture dishes and cultured until forming visible colonies. After isolation and expansion, the DNA was extracted from these clones and genotyping was performed using PCR primers: 5′-GGTTGTCAGACTTGGCT GTG-3′ and 5′-GCAGCTGGACTTTCTGGTTCT-3. Products were sequenced with primer: 5′-ATCTCTTTGTACTGTCTGG-3′ (Eurofins Genomics). mESCs were transduced using viral particles produced by Platinum-E cells, as described above, after transfection with MSCV-IRES-GFP constructs expressing His_{10}-HA-SUMO2. His_{10}-HA-SUMO2 conjugates were purified using NiNTA agarose beads (Qiagen, catalog no. L30210) using Guanidium denaturing lysis as described before (21).

Mouse Model Generation

Pml^{A220V} mice were generated by CRISPR/Cas9 genome editing, performed on BALB/cByJ zygotes using the electroporation method (75). Briefly, 3- to 4-week-old BALB/cByJ females were superovulated using CARD HyperOva (Cosmo bio, #KYD-010-EX) and human chorionic gonadotropin, Sigma; #CG-10) and then mated with males (8–20 weeks) to get zygotes. crRNA, tracrRNA, ssDNA, and Cas9 nuclease were purchased from IDT and electroporated (NEPA21; Sonidal) to introduce Pml point mutation encoding A220V substitution

using Pml target site: 5′-ggttgtcagacttggctgtga-3′ and ssDNA donor sequence: 5′CATCTACTGCCGAGGCTGCGCCAAGCCTCTG TGTTGCACATGCGTGCTCCTCGACCGCAACCACAGCCAT CTCCATTGCG-3′. Genotyping was performed using PCR primers: 5′-GGTTGTCAGACTTGGCTGTG-3′ and 5′-GCAGCTGGACTTTC TGGTTCT-3 and products were sequenced with primer: 5′-ATCT CTTTGTACTGTCTGG-3′ (Eurofins Genomics). This study has been carried out in accordance with national (no. 2013–118) and European (no. 2010/63/UE) directives for animal experiments. Animals were handled according to the guidelines of institutional animal care committees using protocols approved by the "Comité d'Ethique Experimentation Animal Paris-Nord" (no. 121). Animals were housed at our animal facility (UMS Saint-Louis US53/UAR2030, Institut de Recherche Saint-Louis, Paris, France) in accordance with animal welfare and ethical guidelines (accreditation number B75–10–08).

In Vivo *Oxidative Stress Induction Models*

For the transcriptomic study, an early oxidative stress model was used. A female mice cohort (8–10 weeks) were treated with one intraperitoneal (i.p.) injections of 20% carbon tetrachloride CCl_4 (Sigma, catalog no. 289116) diluted in mineral oil (Sigma, catalog no. M8410) or one intraperitoneal injection of mineral oil (2,5 μL/g, $n = 5$ for each group). Mice were sacrificed 18 hours after injections and livers were dissected as follows: left median lobes were stored in RNAlater solution (Invitrogen, catalog no. AM7021) before RNA extraction, right median lobes were frozen in tissue freezing medium (Leica Biosystems, catalog no. 14020108926), right lobes were frozen in liquid nitrogen for protein extraction, and left lobes were fixed in AFA fixative solution (VWR, catalog no. 11656713) for 24 hours and embedded in paraffin for histology staining.

To study a model of longer oxidative stress induction, liver fibrosis was triggered on a female cohort by using 5 weeks treatment of 20% CCl_4, two intraperitoneal injections per week ($n = 7$ CCl_4-treated, $n = 3$ oil-treated). Mice were sacrificed 48 hours after the last injection, and livers were dissected as follows: right median lobes were frozen in tissue freezing medium and left lobes were fixed in AFA fixative solution, embedded in paraffin. The protocol was approved and performed in accordance with animal welfare and ethical guidelines (accreditation number B75–10–08).

Picrosirius Red Staining and Fibrosis Quantification

To assess the liver fibrosis, paraffin-embedded tissue sections (6 μm) were deparaffinized, rehydrated, and stained during 1 hour in a 0.1% Picrosirius Red homemade solution: Direct80 (Sigma; catalog no. 365548) diluted in an aqueous solution saturated in picric acid. The stained liver sections were washed in acidified water, dehydrated in several ethanol baths, cleared in SubX (Leica Biosystems, catalog no. 3803670E), and mounted with a permanent mounting medium. Each stained slide was scanned using the Zeiss AxioScan 7 (Carl Zeiss Micro-Imaging). The red collagen fibers stained by Picrosirius Red solution, were quantified using an open source software, QuPath (76).

RNA Extraction and GeneChip Analysis

Total RNA was extracted using TRIzol (Life Technologies) according to the manufacturer's protocol. Triplicate samples were generated for each genotype, from 3 Pml^{WT}, 3 PML^{KO}, and 3 Pml^{A220V} mice. MTA1.0 Affymetrix Protocol was performed as follows: RNA quantification and quality control was performed using the HT RNA Reagent Kit (Perkin Elmer, catalog no. CLS960010,), the DNA 5KRNA/CZE LabChip (Perkin Elmer, catalog no. 760435), and the Caliper LabChip Microfluidics System (Perkin Elmer, catalog no. GX1133N0432). One-hundred nanograms of total RNA was amplified, labeled, and fragmented using GeneChip Plus Reagent Kit (Thermo Fisher Scientific, catalog no. 902314). Each sample was hybridized onto GeneChip Mouse Transcriptome Array 1.0 (Thermo Fisher Scientific, catalog no. 902514), washed, and stained using the GeneChip Hybridization, Wash, and Stain Kit (Thermo Fisher Scientific, catalog no. 900720) and the Affymetrix Fluidics Station 450 (Thermo Fisher Scientific, catalog no. 60110150). Array scanning was performed with the Affymetrix GeneChip Scanner 3000 7G (Thermo Fisher Scientific, catalog no. 54714280), using the Command Console software (Thermo Fisher Scientific) and then analyzed using the Affymetrix rma-sketch routine [Transcriptome Analysis Console (TAC) software v.4.0.1, Thermo Fisher Scientific]. Raw microarray data (CEL files) were corrected for background, $\log_2$-transformed, and normalized using the standard method RMA (robust multiarray average) implemented in the oligo package (77). Quantile normalization was then applied to mitigate the effects of technical variables using Limma package (78) and probe sets were annotated using mta10transcriptcluster.db package. A linear model fitted in Limma package was performed to identify differential gene expression between Pml^{A220V} versus Pml^{WT} or Pml^{KO} versus Pml^{WT} in basal conditions and after 18 hours of CCl_4 treatment. Differentially expressed genes were identified on the basis of the $P_{adj} < 0.05$ and filtered with a fold change absolute value >2. GSEA were then performed to identify significant hallmark gene sets using the fgsea and msigdbr packages.

Statistical Analysis

Statistical tests performed with GraphPad prism are indicated in the figure legends. Kruskal–Wallis test was used to determine the P value and look for significant changes in PML dynamics at NBs in Pml^{KO} fibroblasts stably expressing GFP-PML. All data are expressed as mean ± SD of technical or biological replicates as indicated. For all graphs, *, $P = 0.01$–0.05, **, $P = 0.001$–0.01, and ***, $P < 0.001$.

Data Availability Statement

Experimentally determined 3D structures can be found from the Protein Data Bank (PDB ID: 8J2P and 8J25). Sources for reagents and cells are indicated in Supplementary Tables S2 and S3. Primary transcriptomic data are accessible on ArrayExpress (accession ID: E-MTAB-13183). The data generated in this study are available upon request from the corresponding authors.

Authors' Disclosures

P. Bercier reports other support from Fondation ARC pour la recherche sur le cancer during the conduct of the study. H. de Thé reports grants from ERC, College de France, INSERM, CNRS, Université Paris Cité, and Institut National du Cancer during the conduct of the study, as well as personal fees from SYROS outside the submitted work. V. Lallemand-Breitenbach reports grants from ITMO Cancer of Aviesan, Collège France, INSERM, and CNRS during the conduct of the study. No disclosures were reported by the other authors.

Authors' Contributions

P. Bercier: Resources, data curation, investigation, visualization, methodology. **Q.Q. Wang:** Resources, data curation, investigation, visualization, methodology. **N. Zang:** Resources, investigation. **J. Zhang:** Resources, investigation. **C. Yang:** Resources, investigation. **Y. Maimaitiyiming:** Resources, investigation. **M. Abou-Ghali:** Resources, investigation, visualization. **C. Berthier:** Resources, investigation. **C. Wu:** Resources, investigation. **M. Niwa-Kawakita:** Resources, investigation. **T. Dirami:** Resources, investigation. **M.-C. Geoffroy:** Resources, investigation. **O. Ferhi:** Resources, formal analysis, methodology. **S. Quentin:** Resources, formal analysis, investigation. **S. Benhenda:** Resources, investigation. **Y. Ogra:** Resources, formal analysis, investigation. **Z. Gueroui:** Resources, formal analysis, funding acquisition, validation. **C. Zhou:** Resources, supervision, funding acquisition, validation, investigation, *writing–original draft*, writing–review and editing. **H. Naranmandura:** Resources, supervision, funding acquisition, validation, investigation, writing–original

draft, writing–review and editing. **H. de Thé:** Resources, supervision, funding acquisition, validation, investigation, writing–original draft, writing–review and editing. **V. Lallemand-Breitenbach:** Resources, supervision, funding acquisition, validation, investigation, writing–original draft, writing–review and editing.

Acknowledgments

The authors acknowledge the Orion technical core of CIRB (Tristan Piolot) for their support on STED analysis (Julien Dumont), and the image analysis on QuPath (Gaëlle Letort, Héloïse Monnet, Philippe Mailly), as well as the histology core facility (Estelle Anceaume), and Magali Fradet for cell sorting support. The authors also thank the UMS Saint Louis US53/UAR2030, Université Paris Cité - INSERM - CNRS, Institut de Recherche Saint-Louis (Niclas Setterblad) for the microarray analysis, and the zootechnicians and Véronique Parietti for taking care of animal models on the "Plateforme d'investigation pré-clinique" and the staff at SSRF BL19U1 for X-ray diffraction data collection and the staff at the National Facility for Protein Science in Shanghai (NFPS) for their help with SEC-MALS experiments. We thank Raphaël Rodriguez (Institut Curie, Paris) for help and advice on peptides/arsenic interactions. The authors thank their funding supports, INSERM, CNRS and Collège de France (to H. de Thé. and V. Lallemand-Breitenbach), Université Paris Cité (to H. de Thé), ITMO Cancer of Aviesan within the framework of the 2021–2030 Cancer Control Strategy, on funds administered by Inserm (PCSI C22028DS, to V. Lallemand-Breitenbach; 22CP117, to Z. Gueroui), Fondation du Collège de France, European Research Council Advanced Grant 785917–PML-THERAPY, the Sjöberg Award (to H. de Thé), Fondation ARC pour la Recherche sur le Cancer (ARC to Pierre Bercier), National Science Foundation of China (82170143, to H. Naranmandura; 31971125, to C. Zhou), and Zhejiang Innovation Team Grant (2020R01006, to H. Naranmandura).

The publication costs of this article were defrayed in part by the payment of publication fees. Therefore, and solely to indicate this fact, this article is hereby marked "advertisement" in accordance with 18 USC section 1734.

Note

Supplementary data for this article are available at Cancer Discovery Online (http://cancerdiscovery.aacrjournals.org/).

Received April 16, 2023; revised July 31, 2023; accepted August 30, 2023; published first September 1, 2023.

REFERENCES

1. Lallemand-Breitenbach V, de The H. PML nuclear bodies: from architecture to function. Curr Opin Cell Biol 2018;52:154–61.
2. Hsu KS, Kao HY. PML: regulation and multifaceted function beyond tumor suppression. Cell Biosci 2018;8:5.
3. de The H, Pandolfi PP, Chen Z. Acute promyelocytic leukemia: a paradigm for oncoprotein-targeted cure. Cancer Cell 2017;32:552–60.
4. Gurrieri C, Nafa K, Merghoub T, Bernardi R, Capodieci P, Biondi A, et al. Mutations of the PML tumor suppressor gene in acute promyelocytic leukemia. Blood 2004;103:2358–62.
5. Koken MHM, Linares-Cruz G, Quignon F, Viron A, Chelbi-Alix MK, Sobczak-Thépot J, et al. The PML growth-suppressor has an altered expression in human oncogenesis. Oncogene 1995;10:1315–24.
6. Mathews V, George B, Chendamarai E, Lakshmi KM, Desire S, Balasubramanian P, et al. Single-agent arsenic trioxide in the treatment of newly diagnosed acute promyelocytic leukemia: long-term follow-up data. J Clin Oncol 2010;28:3866–71.
7. Mathews V, George B, Lakshmi KM, Viswabandya A, Bajel A, Balasubramanian P, et al. Single-agent arsenic trioxide in the treatment of newly diagnosed acute promyelocytic leukemia: durable remissions with minimal toxicity. Blood 2006;107:2627–32.
8. Jeanne M, Lallemand-Breitenbach V, Ferhi O, Koken M, Le Bras M, Duffort S, et al. PML/RARA oxidation and arsenic binding initiate the antileukemia response of As_2O_3. Cancer Cell 2010;18:88–98.
9. Zhang XW, Yan XJ, Zhou ZR, Yang FF, Wu ZY, Sun HB, et al. Arsenic trioxide controls the fate of the PML-RARalpha oncoprotein by directly binding PML. Science 2010;328:240–3.
10. Lallemand-Breitenbach V, Jeanne M, Benhenda S, Nasr R, Lei M, Peres L, et al. Arsenic degrades PML or PML-RARalpha through a SUMO-triggered RNF4/ubiquitin-mediated pathway. Nat Cell Biol 2008;10:547–55.
11. Banani SF, Lee HO, Hyman AA, Rosen MK. Biomolecular condensates: organizers of cellular biochemistry. Nat Rev Mol Cell Biol 2017;18:285–98.
12. Shin Y, Berry J, Pannucci N, Haataja MP, Toettcher JE, Brangwynne CP. Spatiotemporal control of intracellular phase transitions using light-activated optoDroplets. Cell 2017;168:159–71.
13. Mehta S, Zhang J. Liquid-liquid phase separation drives cellular function and dysfunction in cancer. Nat Rev Cancer 2022;22:239–52.
14. Mann JR, Donnelly CJ. RNA modulates physiological and neuropathological protein phase transitions. Neuron 2021;109:2663–81.
15. Ahn JH, Davis ES, Daugird TA, Zhao S, Quiroga IY, Uryu H, et al. Phase separation drives aberrant chromatin looping and cancer development. Nature 2021;595:591–5.
16. Chong S, Graham TGW, Dugast-Darzacq C, Dailey GM, Darzacq X, Tjian R. Tuning levels of low-complexity domain interactions to modulate endogenous oncogenic transcription. Mol Cell 2022;82:2084–97.
17. Banani SF, Rice AM, Peeples WB, Lin Y, Jain S, Parker R, et al. Compositional control of phase-separated cellular bodies. Cell 2016;166:651–63.
18. Sahin U, Ferhi O, Jeanne M, Benhenda S, Berthier C, Jollivet F, et al. Oxidative stress-induced assembly of PML nuclear bodies controls sumoylation of partner proteins. J Cell Biol 2014;204:931–45.
19. Barroso-Gomila O, Trulsson F, Muratore V, Canosa I, Merino-Cacho L, Cortazar AR, et al. Identification of proximal SUMO-dependent interactors using SUMO-ID. Nat Commun 2021;12:6671.
20. Stadler M, Chelbi-Alix MK, Koken MHM, Venturini L, Lee C, Saïb A, et al. Transcriptional induction of the PML growth suppressor gene by interferons is mediated through an ISRE and a GAS element. Oncogene 1995;11:2565–73.
21. Tessier S, Ferhi O, Geoffroy MC, Gonzalez-Prieto R, Canat A, Quentin S, et al. Exploration of nuclear body-enhanced sumoylation reveals that PML represses 2-cell features of embryonic stem cells. Nat Commun 2022;13:5726.
22. Brangwynne CP, Eckmann CR, Courson DS, Rybarska A, Hoege C, Gharakhani J, et al. Germline P granules are liquid droplets that localize by controlled dissolution/condensation. Science 2009;324:1729–32.
23. Brangwynne CP, Mitchison TJ, Hyman AA. Active liquid-like behavior of nucleoli determines their size and shape in Xenopus laevis oocytes. Proc Natl Acad Sci U S A 2011;108:4334–9.
24. Kim J, Han KY, Khanna N, Ha T, Belmont AS. Nuclear speckle fusion via long-range directional motion regulates speckle morphology after transcriptional inhibition. J Cell Sci 2019;132:jcs226563.
25. Weidtkamp-Peters S, Lenser T, Negorev D, Gerstner N, Hofmann TG, Schwanitz G, et al. Dynamics of component exchange at PML nuclear bodies. J Cell Sci 2008;121(Pt 16):2731–43.
26. Geoffroy MC, Jaffray EG, Walker KJ, Hay RT. Arsenic-induced SUMO-dependent recruitment of RNF4 into PML nuclear bodies. Mol Biol Cell 2010;21:4227–39.
27. Daniel M-T, Koken M, Romagné O, Barbey S, Bazarbachi A, Stadler M, et al. PML protein expression in hematopoietic and acute promyelocytic leukemia cells. Blood 1993;82:1858–67.
28. Echaniz-Laguna A, Benoilid A, Vinzio S, Fornecker LM, Lannes B, Goulle JP, et al. Mitochondrial myopathy caused by arsenic trioxide therapy. Blood 2012;119:4272–4.
29. Flora SJ. Arsenic-induced oxidative stress and its reversibility following combined administration of N-acetylcysteine and meso 2,3-dimercaptosuccinic acid in rats. Clin Exp Pharmacol Physiol 1999;26:865–9.
30. Han MJ, Hao J, Christodoulatos C, Korfiatis GP, Wan LJ, Meng X. Direct evidence of arsenic(III)-carbonate complexes obtained using

electrochemical scanning tunneling microscopy. Anal Chem 2007;79:3615–22.
31. Reymond A, Meroni G, Fantozzi A, Merla G, Cairo S, Luzi L, et al. The tripartite motif family identifies cell compartments. EMBO J 2001;20:2140–51.
32. Weerapana E, Wang C, Simon GM, Richter F, Khare S, Dillon MB, et al. Quantitative reactivity profiling predicts functional cysteines in proteomes. Nature 2010;468:790–5.
33. Wu HC, Rerolle D, Berthier C, Hleihel R, Sakamoto T, Quentin S, et al. Actinomycin D targets NPM1c-primed mitochondria to restore PML-driven senescence in AML therapy. Cancer Discov 2021;11:3198–213.
34. Lallemand-Breitenbach V, Zhu J, de The H. Promyelocytic leukemia, a unique model to design treatments targeting oncogenes. Médecine/Sciences 2001;17:14–22.
35. Goto E, Tomita A, Hayakawa F, Atsumi A, Kiyoi H, Naoe T. Missense mutations in PML-RARA are critical for the lack of responsiveness to arsenic trioxide treatment. Blood 2011;118:1600–9.
36. Zhu HH, Qin YZ, Huang XJ. Resistance to arsenic therapy in acute promyelocytic leukemia. N Engl J Med 2014;370:1864–6.
37. Lehmann-Che J, Bally C, de The H. Resistance to therapy in acute promyelocytic leukemia. N Engl J Med 2014;371:1170–2.
38. Iaccarino L, Ottone T, Divona M, Cicconi L, Cairoli R, Voso MT, et al. Mutations affecting both the rearranged and the unrearranged PML alleles in refractory acute promyelocytic leukaemia. Br J Haematol 2016;172:909–13.
39. Wagner JM, Roganowicz MD, Skorupka K, Alam SL, Christensen D, Doss G, et al. Mechanism of B-box 2 domain-mediated higher-order assembly of the retroviral restriction factor TRIM5alpha. Elife 2016;5:e16309.
40. Stoll GA, Oda SI, Chong ZS, Yu M, McLaughlin SH, Modis Y. Structure of KAP1 tripartite motif identifies molecular interfaces required for retroelement silencing. Proc Natl Acad Sci U S A 2019;116:15042–51.
41. Wang QQ, Zhou XY, Zhang YF, Bu N, Zhou J, Cao FL, et al. Methylated arsenic metabolites bind to PML protein but do not induce cellular differentiation and PML-RARalpha protein degradation. Oncotarget 2015;6:25646–59.
42. Muller S, Miller WH, Dejean A. Trivalent antimonials induce degradation of the PML-RAR oncoprotein and reorganization of the promyelocytic leukemia nuclear bodies in acute promyelocytic leukemia NB4 cells. Blood 1998;92:4308–16.
43. Lallemand-Breitenbach V, Zhu J, Puvion F, Koken M, Honore N, Doubeikovsky A, et al. Role of promyelocytic leukemia (PML) sumolation in nuclear body formation, 11S proteasome recruitment, and As(2)O(3)-induced PML or PML/retinoic acid receptor alpha degradation. J Exp Med 2001;193:1361–72.
44. Koken MHM, Puvion-Dutilleul F, Guillemin MC, Viron A, Linares-Cruz G, Stuurman N, et al. The t(15;17) translocation alters a nuclear body in a RA-reversible fashion. EMBO J 1994;13:1073–83.
45. de The H. Differentiation therapy revisited. Nat Rev Cancer 2018;18:117–27.
46. Niwa-Kawakita M, Ferhi O, Soilihi H, Le Bras M, Lallemand-Breitenbach V, de The H. PML is a ROS sensor activating p53 upon oxidative stress. J Exp Med 2017;214:3197–206.
47. Gentric G, Kieffer Y, Mieulet V, Goundiam O, Bonneau C, Nemati F, et al. PML-regulated mitochondrial metabolism enhances chemosensitivity in human ovarian cancers. Cell Metab 2019;29:156–73.
48. Alhazmi N, Pai CP, Albaqami A, Wang H, Zhao X, Chen M, et al. The promyelocytic leukemia protein isoform PML1 is an oncoprotein and a direct target of the antioxidant sulforaphane (SFN). Biochim Biophys Acta Mol Cell Res 2020;1867:118707.
49. Guo L, Giasson BI, Glavis-Bloom A, Brewer MD, Shorter J, Gitler AD, et al. A cellular system that degrades misfolded proteins and protects against neurodegeneration. Mol Cell 2014;55:15–30.
50. Rerolle D, de The H. The PML hub: an emerging actor of leukemia therapies. J Exp Med 2023;220:e20221213.
51. Guo S, Cheng X, Lim JH, Liu Y, Kao HY. Control of antioxidative response by the tumor suppressor protein PML through regulating Nrf2 activity. Mol Biol Cell 2014;25:2485–98.
52. Zhong S, Hu P, Ye TZ, Stan R, Ellis NA, Pandolfi PP. A role for PML and the nuclear body in genomic stability. Oncogene 1999;18:7941–7.
53. Krizhanovsky V, Yon M, Dickins RA, Hearn S, Simon J, Miething C, et al. Senescence of activated stellate cells limits liver fibrosis. Cell 2008;134:657–67.
54. Shen TH, Lin HK, Scaglioni PP, Yung TM, Pandolfi PP. The mechanisms of PML-nuclear body formation. Mol Cell 2006;24:331–9.
55. Shen S, Li XF, Cullen WR, Weinfeld M, Le XC. Arsenic binding to proteins. Chem Rev 2013;113:7769–92.
56. Zhang HN, Yang L, Ling JY, Czajkowsky DM, Wang JF, Zhang XW, et al. Systematic identification of arsenic-binding proteins reveals that hexokinase-2 is inhibited by arsenic. Proc Natl Acad Sci U S A 2015;112:15084–9.
57. Ablain J, Rice K, Soilihi H, de Reynies A, Minucci S, de The H. Activation of a promyelocytic leukemia-tumor protein 53 axis underlies acute promyelocytic leukemia cure. Nat Med 2014;20:167–74.
58. Vitaliano-Prunier A, Halftermeyer J, Ablain J, de Reynies A, Peres L, Le Bras M, et al. Clearance of PML/RARA-bound promoters suffice to initiate APL differentiation. Blood 2014;124:3772–80.
59. Dagher T, Maslah N, Edmond V, Cassinat B, Vainchenker W, Giraudier S, et al. JAK2V617F myeloproliferative neoplasm eradication by a novel interferon/arsenic therapy involves PML. J Exp Med 2021;218:e20201268.
60. Datta N, Chakraborty S, Basu M, Ghosh MK. Tumor suppressors having oncogenic functions: the double agents. Cells 2020;10:46.
61. Carracedo A, Weiss D, Leliaert AK, Bhasin M, de Boer VC, Laurent G, et al. A metabolic prosurvival role for PML in breast cancer. J Clin Invest 2012;122:3088–100.
62. Zhu J, Chen Z, Lallemand-Breitenbach V, de Thé H. How acute promyelocytic leukemia revived arsenic. Nat Rev Cancer 2002;2:705–13.
63. de The H, Chen Z. Acute promyelocytic leukaemia: novel insights into the mechanisms of cure. Nat Rev Cancer 2010;10:775–83.
64. Madeira F, Pearce M, Tivey ARN, Basutkar P, Lee J, Edbali O, et al. Search and sequence analysis tools services from EMBL-EBI in 2022. Nucleic Acids Res 2022;50(W1):W276–W9.
65. Zhu J, Zhou J, Peres L, Riaucoux F, Honore N, Kogan S, et al. A sumoylation site in PML/RARA is essential for leukemic transformation. Cancer Cell 2005;7:143–53.
66. Garcia-Jove Navarro M, Kashida S, Chouaib R, Souquere S, Pierron G, Weil D, et al. RNA is a critical element for the sizing and the composition of phase-separated RNA-protein condensates. Nat Commun 2019;10:3230.
67. Sprague BL, Pego RL, Stavreva DA, McNally JG. Analysis of binding reactions by fluorescence recovery after photobleaching. Biophys J 2004;86:3473–95.
68. Evans PR, Murshudov GN. How good are my data and what is the resolution? Acta Crystallogr D Biol Crystallogr 2013;69(Pt 7):1204–14.
69. Kabsch W. Xds. Acta Crystallogr D Biol Crystallogr 2010;66(Pt 2):125–32.
70. Winn MD, Ballard CC, Cowtan KD, Dodson EJ, Emsley P, Evans PR, et al. Overview of the CCP4 suite and current developments. Acta Crystallogr D Biol Crystallogr 2011;67(Pt 4):235–42.
71. McCoy AJ, Grosse-Kunstleve RW, Adams PD, Winn MD, Storoni LC, Read RJ. Phaser crystallographic software. J Appl Crystallogr 2007;40(Pt 4):658–74.
72. Emsley P, Cowtan K. Coot: model-building tools for molecular graphics. Acta Crystallogr D Biol Crystallogr 2004;60(Pt 12 Pt 1):2126–32.
73. Liebschner D, Afonine PV, Baker ML, Bunkoczi G, Chen VB, Croll TI, et al. Macromolecular structure determination using X-rays, neutrons and electrons: recent developments in Phenix. Acta Crystallogr D Struct Biol 2019;75(Pt 10):861–77.
74. Jumper J, Evans R, Pritzel A, Green T, Figurnov M, Ronneberger O, et al. Highly accurate protein structure prediction with AlphaFold. Nature 2021;596:583–9.
75. Hashimoto M, Takemoto T. Electroporation enables the efficient mRNA delivery into the mouse zygotes and facilitates CRISPR/Cas9-based genome editing. Sci Rep 2015;5:11315.
76. Bankhead P, Loughrey MB, Fernandez JA, Dombrowski Y, McArt DG, Dunne PD, et al. QuPath: Open source software for digital pathology image analysis. Sci Rep 2017;7:16878.
77. Carvalho BS, Irizarry RA. A framework for oligonucleotide microarray preprocessing. Bioinformatics 2010;26:2363–7.
78. Ritchie ME, Phipson B, Wu D, Hu Y, Law CW, Shi W, et al. limma powers differential expression analyses for RNA-sequencing and microarray studies. Nucleic Acids Res 2015;43:e47.